Thesis for the Degree of Doctor of Philosophy

On Super Bright Transparent Film Phosphors

by

Je Hong Park

Department of Image Science and Engineering,

The Graduate School,

Pukyong National University

January 2011

On Super Bright Transparent Film Phosphors

(고휘도 투명 필름형광체 연구)

Advisor: Prof. Jong Su Kim

by

Je Hong Park

A thesis submitted in partial fulfillment of the requirements
for the degree of Doctor of Philosophy

in Department of Image Science and Engineering, The Graduate School, Pukyong National University

January 2011

박재홍의 박사 학위논문을 인준함

2010년 12월 일

주 심	정 용 석	(인)
위 원	김 종 수	(인)
위 원	정 연 태	(인)
위 원	유 일	(인)
위 원	유 영 문	(인)

CONTENTS

LIST OF FIGURES

ABSTRACT

The film phosphors were prepared by thermal-diffusion reactions between quartz substrate and film materials which are spin-coated. Silicate-based film phosphors (Zn_2SiO_4:Mn^{2+} and $BaSi_2O_5$:Eu^{2+}) using a quartz (SiO_2) substrate and film materials (ZnO:Mn and BaO:Eu) are synthesized in this thesis. Their optical properties were investigated with annealing conditions and dopant (Mn and Eu) concentrations. From X-ray diffraction (XRD) analysis and scanning electron microscope (SEM), we confirmed that film phosphors on substrate were successfully formed and revealed the following characteristics.

The Zn_2SiO_4:Mn^{2+} film phosphor (thickness = 1μm) became textured along several special hexagonal directions [(113), (223), (333) crystal plane] and their chemical compositions were continuously graded at the interface. The brightest Zn_2SiO_4:Mn^{2+} film (Mn/Zn = 5 at.%) showed a photoluminescent brightness as high as 65 % and 40 % compared with a commercial Zn_2SiO_4:Mn^{2+} phosphor powder screen at the same weigh excited by 254 nm UV lamp and 147 nm VUV, respectively and it has short decay time of 4.4 ms, and maximum absolute transparency of 70%.

The Zn_2SiO_4:Mn^{2+} phosphor shell (5 μm) coated on SiO_2 powder (100~200 μm) showed a short decay time ($\tau_{10\%}$ = 7.3 ms)

compared to that of a powder phosphor ($\tau_{10\%}$ = 12 ms) synthesized through a conventional method at same Mn^{2+} concentration.

The $BaSi_2O_5:Eu^{2+}$ film phosphor (thickness = 800 nm) revealed some preferred-orientation crystalline [(110), (111), (204) crystal plane]. The $BaSi_2O_5:Eu^{2+}$ thin-film phosphor (Eu/Ba = 11 at.%) showed bright green emission and it has a high transparency of 75 %.

Keywords : Film phosphor, transparency

1. INTRODUCTION

Phosphors are composed of a wide-band gap host crystal and a luminescent center called an activator, i.e., a small amount of intentionally added impurity atoms distributed in host crystal[1-2].

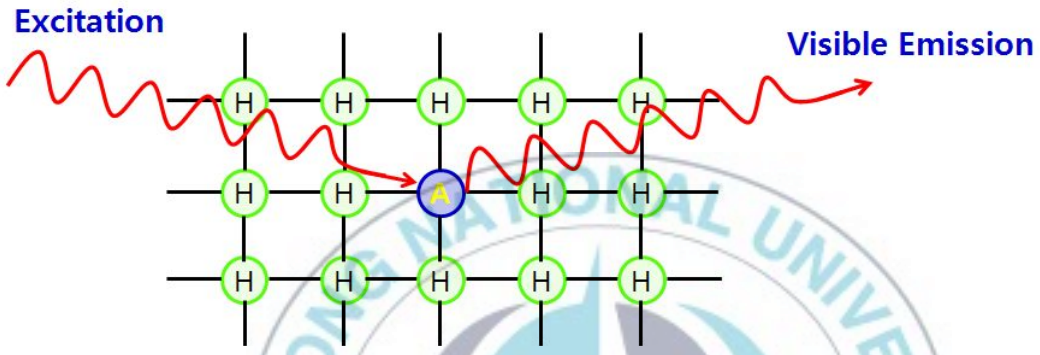

Figure 1. Schematic structure of host crystal (H) and activator (A) in host crystal.

Figure 1 shows schematic system of a phosphor. The luminescence processes in such a system are as follows. Excitation sources such as photon, accelerated electron, electric field are absorbed by the activator, raising it to an excited state. The excited state returns to the ground state by emission of radiation as seen in figure 2.

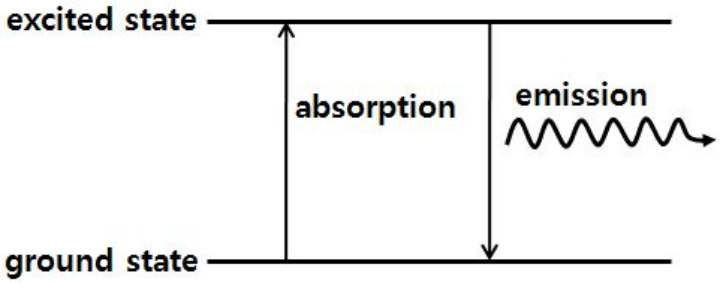

Figure 2. Schematic energy level of the activator.

Phosphors have been used for a means of displaying of information since the invention of the cathode-ray tube (CRT) by Braun in 1897 [3]. The most signigicant advances in phosphor technology came with the advent of color television. White brightness efficiency of phosphor screens also improved significantly: 15 lm/W in 1951 to over 35 lm/W in 1979, as a results of new phosphor formulations and improved screening techniques [4-5].

There has been interest in the development of film phosphors for flat panel displays. Film phosphors have several advantages such as long-term stability, high image resolution, thermal stability, good heat resistance, and superior adhesion to the substrate compared to powder phosphors[6-8].

In this thesis, bright and transparent film phosphor ($Zn_2SiO_4:Mn^{2+}$ and $BaSi_2O_5:Eu^{2+}$) using a simple method through

thermally diffused reaction between quartz (SiO_2) substrate and spin-coated thin film materials (ZnO:Mn and BaO:Eu) on quartz (SiO_2) substrate. Formed film phosphors through this method show dense, low density of pore and grain-boundary in appearance. They have unique crystalline structure with some preferred crystal orientations. Optical properties could be affected by these factors. In addition, luminescence properties $Zn_2SiO_4:Mn^{2+}$ phosphor shell on surface of SiO_2 powder were investigated.

Chapter 2 and 3 will provide a theory of luminescence and survey of recent research development for film phosphor with $Zn_2SiO_4:Mn^{2+}$, $BaSi_2O_5:Eu^{2+}$ phosphors, respectively. Experimental procedures for film phosphors and phosphor shell will be presented in chapter 4. The results and discussion of $Zn_2SiO_4:Mn^{2+}$, $Zn_2SiO_4:Mn^{2+}$ phosphor shel and $IBaSi_2O_5:Eu^{2+}$ film phosphors are presented in chapter 5. Chapter 6 provides a summary of this study.

2. THEORY

Atomic transitions are influenced by the host lattice material, because they are localized radiative events between atomic states associated with the luminescent center. Atomic transitions depends primarily on the electronic states involved in the transition. Here we will discuss how the host material interacts with the luminescent center, and discuss specifically how the transition energy depends on the local environment : symmetry, bond length and molecular orbital overlap [9]. Also we will discuss the optimum concentration of a host and the energy transfer mechanism from the excited center to another center.

2.1. Symmetry

The symmetry is associated with the specific lattice position of the luminescent center. When introduced into a pseudo-ionic solid, a transition metal or rare earth ion substitutes for a cation site. Therefore, one is interested in how the nearest-neighbour anions are arranged with respect to the cation site. In addition, it is important to understand the shape and symmetry of the electron orbitals involved in the radiative transition. For transition metal ions, d-d intrashell transitions occur, and in rare earth ions, both 4f-5d intershell and 4f-4f intrashell transitions occur[10].

The electronic configurations of transition metal ions are straightforward in that the d-orbitals are the outer orbitals, and are

unshielded by any other electron orbital. By examining the electron configuration of the lanthanide rare earths series, it can easily be shown that the 4f levels are shielded by the 5s and 5p electrons, and are subsequently unaffected by the host lattice.

The shape and symmetry of the d-orbitals have essentially five orientations: the d_{xy}, d_{yz}, and d_{zx} have the same distribution, and the $d_{x^2-y^2}$ and d_{z^2} have unique distributions. The energy level position associated with each orientation depends on how the neighbouring anions are situated. Each orbital orientation has an energy associated with it which is dependent on the orbital-ligand interaction. If one assumes that the anions are simply point charges, then the relative energy positions for each orbital orientation can be estimated. For octahedral symmetry, the $d_{x^2-y^2}$ and d_{z^2} lobes point directly at the anions and the d_{xy}, d_{yz}, and d_{zx} lobes point between anion. Because the anion interaction is stronger for $d_{x^2-y^2}$ and d_{z^2} lobes versus the d_{xy}, d_{yz}, and d_{zx} lobes, and $d_{x^2-y^2}$ and d_{z^2} have a higher energy than the d_{xy}, d_{yz}, and d_{zx} orientations. A similar argument can be applied to the tetrahedral symmetry which demonstrates that for this arrangement, the d_{xy}, d_{yz}, and d_{zx} have a higher energy relative to $d_{x^2-y^2}$ and d_{z^2} orientations. Simple geometric considerations show that the d-opital crystal field splitting (Dq) of the tetrahedral symmetry is 4/9

the magnitude of the octahedral splitting ($Dq(T_d) = 4/9\ Dq(O_h)$) [11]. Figure 3 shows the d-orbital splitting for both the octahedral and tetrahedral symmetry.

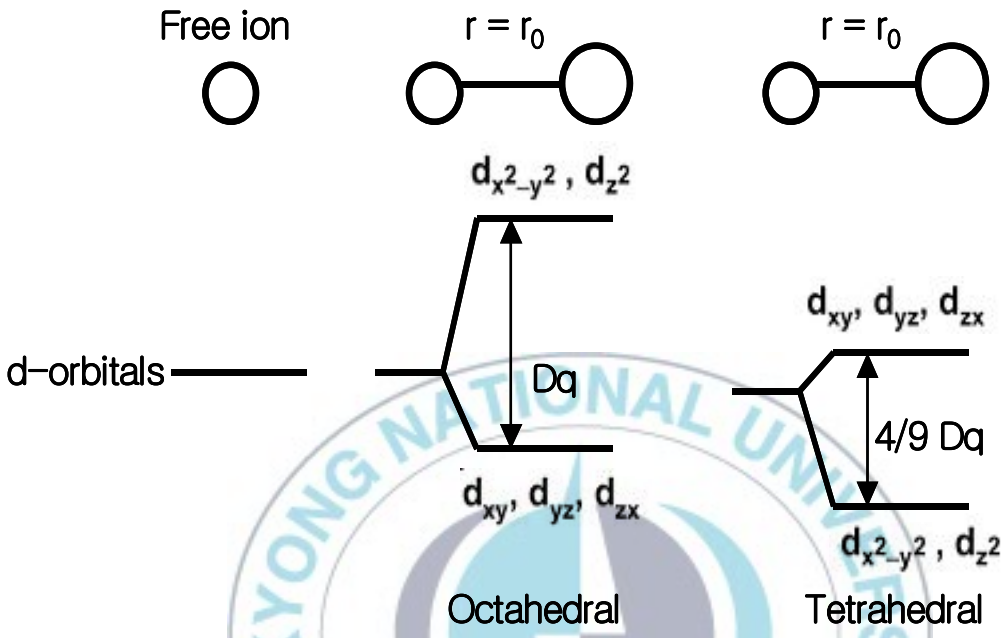

Figure 3. d-orbital splitting for the octahedral and tetrahedral symmetry.

2.2. Bond length

The atomic energy level of the luminescent center are dependent on the bond length of the host material. The bond length dependence of the d-orbital splitting can be easily understood by approximating the ions as point charges and considering the electric field. Applying this same logic to ions in a solid, as the bond length decrease between anions

and cations, the crystall field in the solid increases. Conversely, when the bond length increases, the crystal field decreases and atomic states become more like the free ion case. Also it is possible to consider how the energy levels of rare earth ions are affected by the host lattice bond length.

The results of the " point charge model " can be used to demonstrate how the bond length modifies or splits the d-orbitals. This model represents anions with point charges, and takes into account the radial nature of the d-orbital wavefunction. The point charge model applied to d-orbital splitting results in the simple algebraic expression [12]:

$$Dq = \frac{1}{6} ze^2 \frac{r^4}{a^5} \quad (1)$$

where Dq is the energy level separation, z is the charge or valence of the anion, e is the charge of an electron, r is the radius of the d wavefunction, and a is the bond length. Eq.(1) clearly shows that when a radiative transition involves an outer d-orbital (3d or 5d), the emission color can vary depending on the lattice spacing of the host material. The influence that the bond distance has on the splitting is demonstrated in Figure 4.

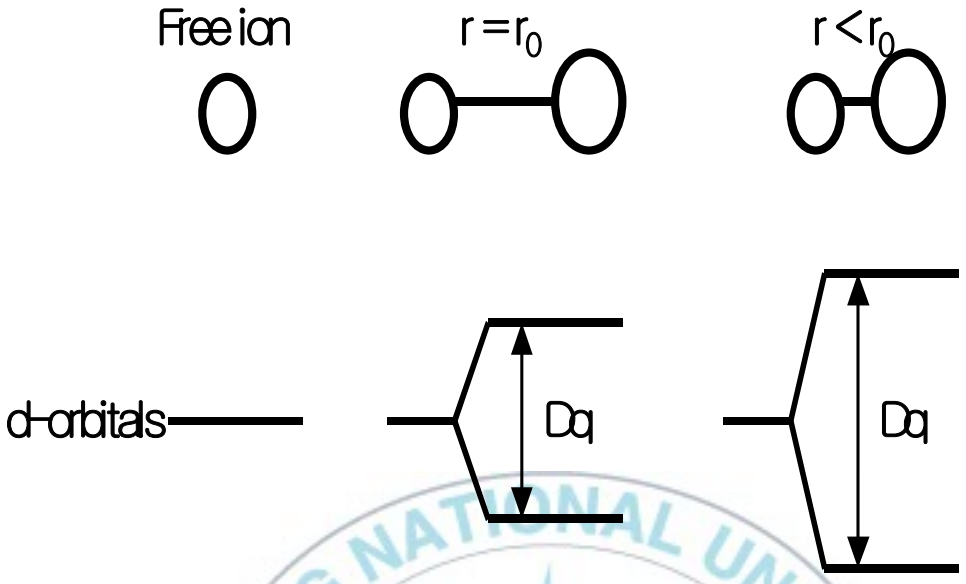

Figure 4. d-orbital splitting for bond length.

2.3. Molecular orbital overlap

The cation and an ion properties of the host lattice influences atomic radiative transitions. These effects are not as intuitive as the symmetry and bond length effects because they is related with cation-anion molecular orbital (MO) overlap. The degree of the MO overlap in a solid depends on the bonding type (ionic vs. covalent); if the bonding is primarily ionic then the MO overlap is small, and if the bonding is primarily covalent then the MO overlap is large. An estimation of the fraction of covalency (f_c) for a given bond is expressed by [13]:

$$f_c = \exp[(-0.25)\Delta EN^2] \quad (2)$$

where ΔEN is difference in the anion and cation electronegativities. Eq. (2) demonstrates that the bonding between two ions is a function of how strong each ion binds its outer electrons. For elemental semiconductors (i.e. Si and Ge) where ΔEN is zero, these solids are characterized as having perfectly covalent bonds, and valence electrons are shared between neighbouring atoms. When the ΔEN increases for III-V and II-VI materials, their bonding becomes more ionic because the anion has a stronger attraction for electrons versus the cation.

In the free ion state, there are obviously no MO interactions and if spin-orbit interactions are ignored, all the d-orbitals are degenerate with respect to energy. However, when these orbitals interact with nearest neighbour anions, the d-orbitals hybridize due to electron cloud interactions. This effect is called the nephelauxetic effect which literally translated means electron cloud expanding[2]. When a transition metal or rare earth ion is surrounded by a host lattice, the normal electron orbital distributions are perturbed and new energy states are produced. The orbital interactions create lower energy bonding states and higher energy antibonding states through hybridization. As the MO overlap increases for more covalent solids, the energy position of the bonding states and antibonding states shifts to lower energy. While the bonding states and

antibonding states may shift by different amounts, if the details of the ground state and the excited state are known one can predict how different host materials (more ionic or more covalent) will change the radiative transition energy of a luminescent center.

2.4. Activator concentration quenching

There is always an optimum activator concentration, but the exact number of sites will vary from host to host[14]. The optimum concentration of one host as a function of the plurality of localized phonon modes will different from other host lattice. This is because the emission intensity(I_{em}) is directly proportional to the number of activator centers(N_A), and is an inversely exponential function of the number of quenching centers(N_Q). These quenching centers may be nearest neighbor activator sites which dissipate energy by direct exchange, or they may be distant sites accessible by resonant exchange mechanisms. This effect is illustrated in figure 5. Initially the emission intensity is linearly proportional to the number of emitting activator sites(N_A) and dI/dx is a constant value.

At quenching point, the density of these sites becomes too large and the overall emission intensity falls exponentially as concentration increases. The reason is that the original nearest neighbors become quenching sites because of direct exchange coupling for the virtual photon exchange mechanism. Thus, if the number of activator sites

increase beyond a specific point, the energy dissipation mechanisms become dominant. The optimum activator concentration is a function of the nature of the activator and the nature of the host is not easily predicted or calculated. It is usually experimentally determined.

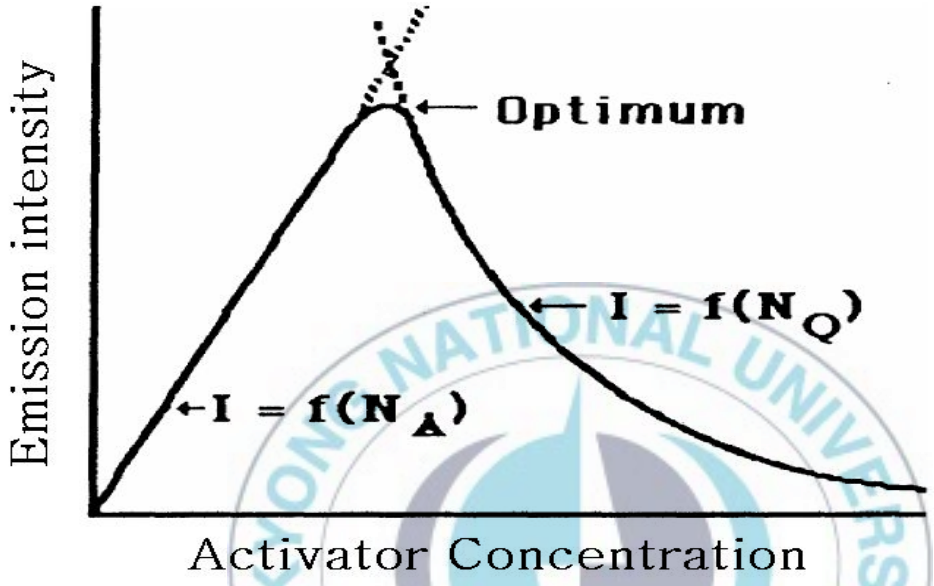

Figure 5. Optimum intensity with activator concentrations.

2.5. Energy Transfer

The possibility to return to the ground state is considered by energy transfer from the excited center (S^*) to another center (A):

$$S^* + A \rightarrow S + A^*$$

If A^* emits light after energy transfer from S^* to A^*, S is said to be a sensitizer of A. However, if A^* may also decay nonradiatively, A is said

to be a quencher. S and A are separated in a solid by distance R. The energy level schemes are also given in figure 6. An asterisk(*) indicates the excited state. Let us assume that the distance R is so short that the centers S and A have a non-vanishing interaction with each other. If S is in the excited state and A in the ground state, the relaxed excited state of S may transfer its energy to A. Energy transfer can only occur if the energy differences between the ground and excited states of S and A are equal i.e., resonance condition, and if a suitable interaction between both systems exists. The interaction may be either an exchange interaction if we have wave function overlap or an electric or magnetic multipolar interaction.

The resonance condition can be tested by considering the spectral overlap of the S emission and the A absorption spectra. The Dexter result looks as follows[12]:

$$P_{SA} = 2/h |\langle S, A^* | H_{SA} | S^*, A \rangle|^2 \int g_s(E) g_A(E) dE \qquad (3)$$

The integral presents the spectral overlap between $g_A(E)$ and $g_S(E)$ being the normalized optical line shape function of center A and S. Eq. (3) shows that the transfer rate P_{SA} vanishes for vanishing spectral overlap.

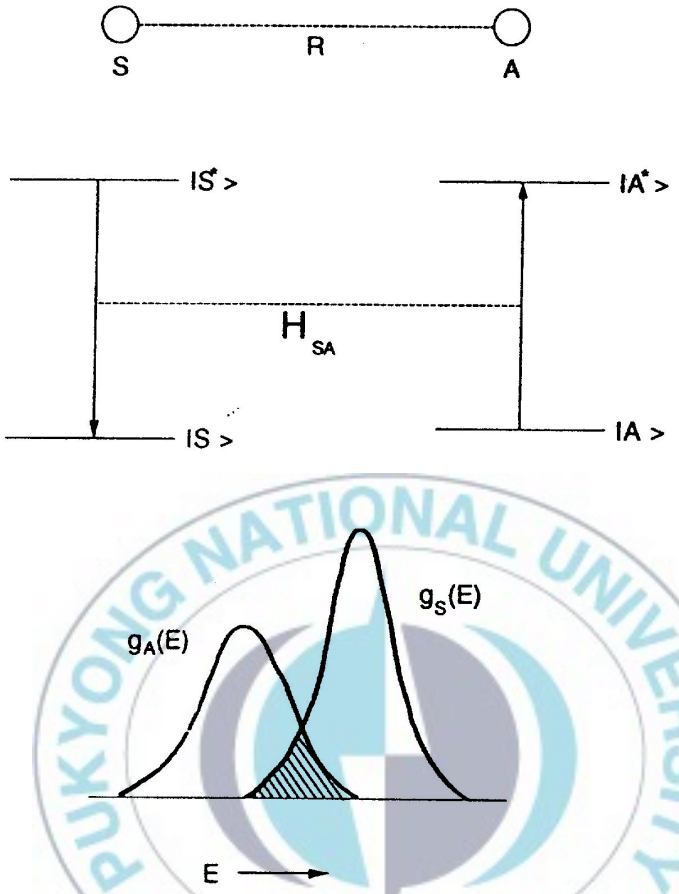

Figure 6. Energy transfer between the centers S and A at a distance R. The spectral overlap is illustrated at the bottom.

The matrix element(H_{SA}) represents the interaction Hamiltonian between the initial state |S*, A > and the final state |S, A* >. The distance dependence of the transfer rate depends on the type of interaction. For electric multipolar interaction the distance dependence is given by R^{-n} (n

= 6, 8,... for electric-dipole electric-dipole interaction, electric-dipole electric-quadrupole interaction,... respectively). For exchange interaction the distance dependence is exponential, since exchange interaction requires wave function overlap. A high transfer rate, i.e., a high value of P_{SA}, requires a considerable amount as follows :

(1) resonance, i.e., the S emission band should overlap spectrally the A absorption band.
(2) interaction of the multipole-multipole type or of the exchange type.

The critical distance for energy transfer (R_c) is defined as the distance for which P_{SA} equals P_S, i.e., if S and A are separated by a distance R_c, the transfer rate equals the radiative rate. For $R > R_c$ radiative emission from S prevails, for $R < R_c$ energy transfer from S to A dominates.

If the optical transitions of S and A are allowed electric-dipole transitions with a considerable spectral overlap, R_c may be some 30 Å. If these transitions are forbidden, exchange interaction for the transfer occurs. This restricts the value of R_c to some 5-8 Å. Assuming that the interaction is of the electric-dipolar type, Eq. (3) together with P_{SA} (R_C) = P_S yields for R_c the following expression:

$$R_c^6 = 3 * 10^{12} f_A E^{-4} \int g_S(E)\, g_S(E)\, dE \qquad (4)$$

Here f_A presents the oscillator strength of the optical absorption transition on A, E the energy of maximum spectral overlap. Eq. (4) makes it possible to calculate R_C from spectral data. In addition, Energy transfer from a broad-band emitter to a line absorber is only possible for nearest neighbours in the crystal lattice, and transfer from a line emitter to a band absorber proceeds over fairly long distances.

The shape of the decay curve is characteristic of the energy transfer processes[2]. A compound of a rare earth ion S contains some ions A, which are able to trap the migrating excitation energy of S by SA transfer.

(a) If excitation into S is followed by emission from the same S ion, or if excitation into S is followed after some migration by emission from S only, the decay is described by

$$I = I_0 \exp(-rt) \qquad (5)$$

where I_0 is the emission intensity at time t = 0, i.e., immediately after the pulse, and r is the radiative rate.

(b) If some SA transfer occurs but no SS transfer at all, the S decay

is given by

$$I = I_0 \exp(rt - Ct^{3/n}) \tag{6}$$

where C is a parameter containing the A concentration and the SA interaction strength, and n (> 6) depends on the nature of the multipolar interaction.

The decay immediately after the pulses faster than in the absence of A. This represents the decay of S ions which do not have A ions in the surroundings.

(c) If Pss >> P_{SA}, the decay rate is exponential and fast as following:

$$I = I_0 \exp(rt - C_A P_{SA} t) \tag{7}$$

(d) If Pss << P_{SA} and dealing with diffusion-limited energy migration, the decay curve for t $\rightarrow\infty$ can be described by

$$I = I_0 \exp(rt - 11.404 C_A C^{1/4} D^{3/4} t) \tag{8}$$

if the sublattice of S ions is three dimensional. C is a parameter

describing the SA interaction and D is the diffusion constant of the migrating excitation energy. For lower dimensions non-exponential decays are to be expected. Figure 7 shows some of these decay curves. The temperature dependence of P_{ss} is very complicated. Due to inhomogeneous broadening, the S ions are not exactly resonant, but their energy levels show very small mismatches. At room temperature, the lines are broadened and phonons are available, so that these mismatches do not hamper the energy migration. However, at very low temperatures they hamper the energy migration, or make it even impossible.

For identical ions, one-phonon assisted processes are not of much importance. Two-phonon assisted processes have a much higher probability. One of these (a two-site nonresonant process) yields a T^3 dependence. Another (a one-site resonant process), which uses a higher energy level gives an $\exp(-\Delta E/kT)$ dependence, where ΔE is the energy difference between the level concerned and the higher level.

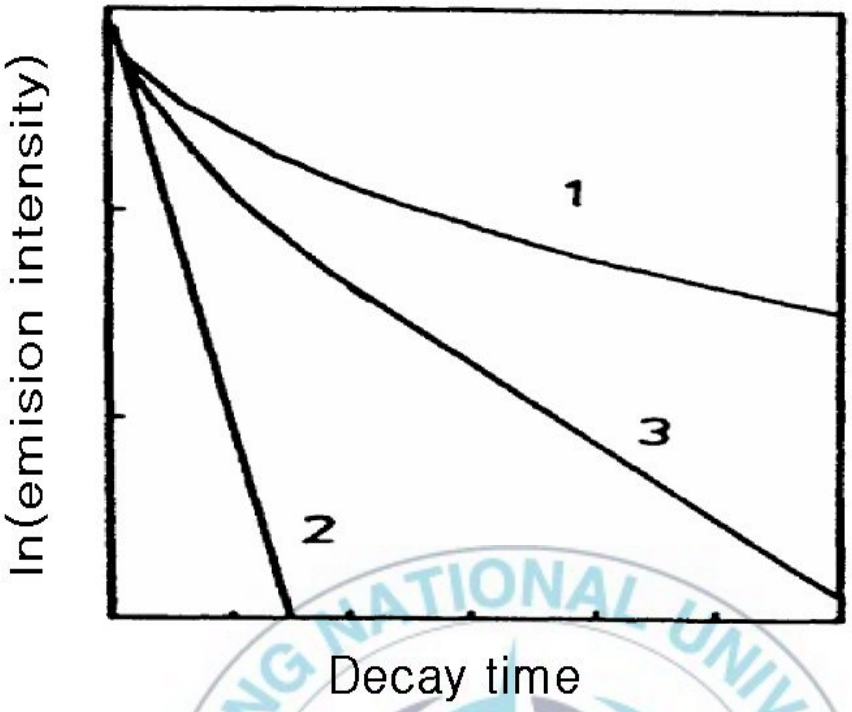

Figure 7. Several possibilities for the decay curve of the excited S ion. Curve 1: no SS transfer; curve 2: rapid SS migration; curve 3: intermediate case.

3. LITERATURE REVIEW

3-1. FILM PHOSPHORS

Film phosphors have several advantage compared to powder phosphors such as reduced outgassing, superior adhesion, high image resolution, good heat resistance, and long-term stability[6-8]. However, film phosphors have poor luminance compared to powder phosphors because of their low external quantum efficiency (η_{ex}). The external quantum efficiency is related to the internal quantum efficiency (η_{in}) and the fraction of light escaping (light extraction efficiency) the film phosphor (η_{esc})[6, 15].

$$\eta_{ex}=\eta_{in} \cdot \eta_{esc}$$

The poor light extraction efficiency (η_{esc}) of film phosphors is associated with factors such as (i) internal reflection at interface between media with different refractive indices, (ii) absorption of generated light by substrate materials[16]. Figure 8 shows propagation of generated light in film phosphor.

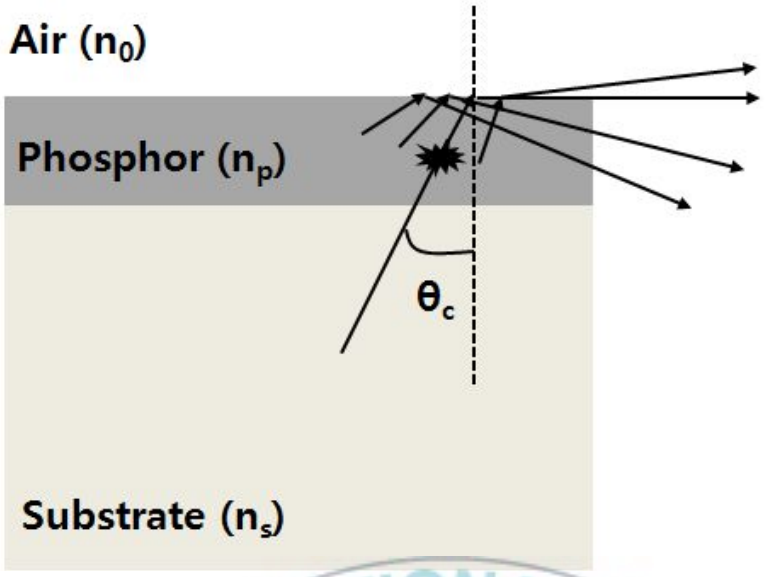

Figure 8. Propagation of light generated in film phosphor.

When light generated in film phosphor reaches the interface having some angle θ_1, the light is refracted according to Snell's law [17]

$$n_p \cdot \sin\theta_1 = n_0 \cdot \sin\theta_2$$

where n_p and n_0 are the refractive index for each media and θ_1 is the incident angle and θ_2 is refraction angle of light at the interface. Let the light pass from a denser medium (higher refractive index : n_p) to a rarer medium (lower refractive index : n_0). As the angle of incidence is gradually made larger, the angle of refraction becomes bent toward the interface. The incident light

is not refracted but is tangent to the surface and $\sin\theta_2$ becomes unity. This incident angle is the limiting angle of refraction at the interface called the critical angle (θ_c) for total internal reflection. Total internal reflection cause poor light extraction efficiency in film phosphors, therefore, methods for enhancement of extraction efficiency in film luminescent materials have been studied by many researchers[6,8,15,18-30]. Some significant improvements of extraction efficiency have been made by modifying the shape and morphology of the surface of film phosphors[6,8,15,18-28]. Chao et al. have also reported that the improved efficiency of film phosphor that results from introducing a metal array onto the film phosphor is due to surface plasmon coupling[29,30].

The internal quantum efficiency (η_{in}) depends on crystallinity of film phosphors[31-33]. Pores and grain boundaries of film phosphor are luminescent killer for radiation at the luminescent center. Therefore, high quality film having low density of pores and grain boundaries is required for enhancement of internal quantum efficiency in film phosphors.

Film phosphors can be fabricated using various techniques, including sputtering deposition[34,35], pulsed laser deposition[16], atomic layer deposition[36] and chemical vapor deposition[37]. However, these methods require expensive and complicated

equipment need to vacuum techniques. One of the simple methods for film phosphors is solution-based spin-coating technique. Spin-coating technique is done in air atmosphere, thus have simple and inexpensive process compared to other vacuum method.

In this thesis, we prepared film phosphor ($Zn_2SiO_4:Mn^{2+}$ and $BaSi_2O_5:Eu^{2+}$) using a simple method through thermally diffused reaction between quartz (SiO_2) substrate and spin-coated thin film materials (ZnO:Mn and BaO:Eu) on quartz (SiO_2) substrate. We have focused on relation between crystalline structure and optical properties of our film phosphors. We have also studied on luminescent properties of $Zn_2SiO_4:Mn^{2+}$ phosphor shell.

3-2. $Zn_2SiO_4:Mn^{2+}$ phosphor

Zinc silicate is wellimite crystal structure which have Zn-O, Si-O bonding and networked by oxygen as seen in figure 9 [38]. The host matrix for many rare earth and transition metal dopant ions for the efficient luminescence. This host system has the chemical stability and semi-conducting properties[39,40]. A prominent green emission color has been reported on $Zn_2SiO_4:Mn^{2+}$ phopsphors[40, 41]. $Zn_2SiO_4:Mn^{2+}$ is widely used in display devices such as plasma display panels (PDPs), vacuum fluorescence displays (VFDs), electroluminescence device (ELD) and cathode ray

tubes (CRTs)[1,42,43]. It is well know that Zn^{2+} and Mn^{2+} ions have similar oxidation states and their radii being similar and therefore Mn^{2+} ions could be well distributed as the substitutions of Zn^{2+} in the Zn_2SiO_4 host matrix and hence encouraging a strong green emission band at 525 nm due to the $^4T_1$–$^6A_1$ transition of the Mn^{2+} ions[40, 44].

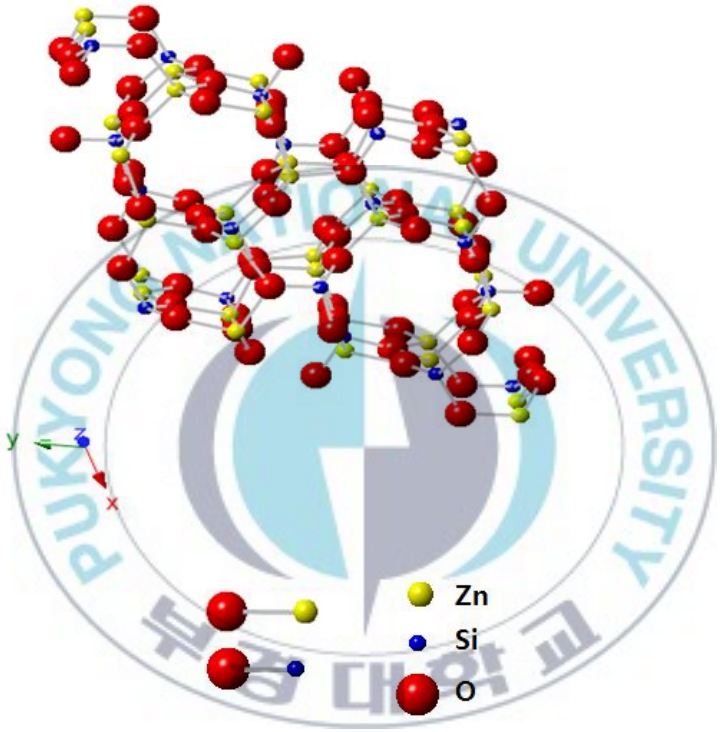

Figure 9. Crystal structure of Zn_2SiO_4.

3-3. $BaSi_2O_5:Eu^{2+}$ phosphor

Barium silicate is sanbornite crystal structure which have Ba-O, Si-O bonding and networked by oxygen as seen in figure 10 [45]. Eu^{2+} ions could be well distributed as the substitutions of Ba^{2+} in the $BaSi_2O_5$ host matrix and hence encouraging a green emission band at 508 nm due to the f-d transition of the Eu^{2+} ions[46-48].

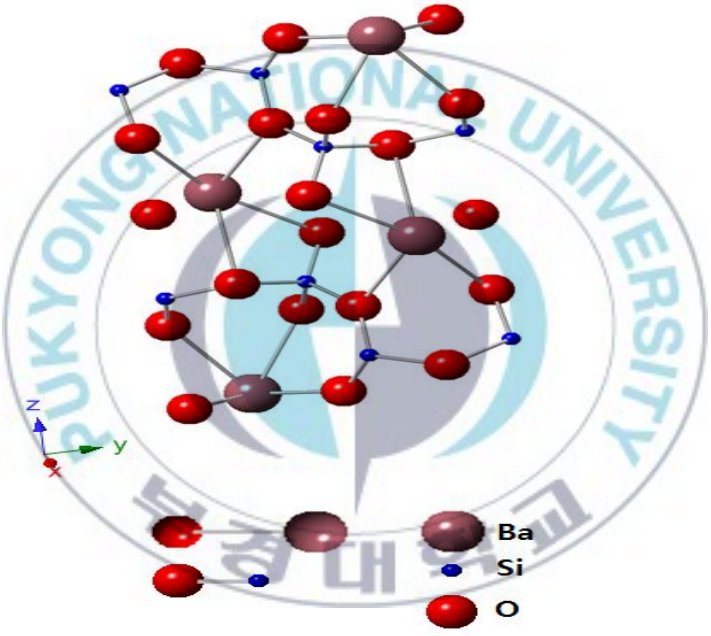

Figure 10. Crystal structure of $BaSi_2O_5$.

4. EXPERIMENTAL PROCEDURES

4.1. $Zn_2SiO_4:Mn^{2+}$ FILM PHOSPHOR

1 M sol-gel solution of ZnO:Mn was prepared for spin coating using the following procedure. Zinc acetate dehydrate [$Zn(CH_3COO)_2 2H_2O$] was first dissolved in isopropanol [$(CH_3)_2CHOH$]-monoethanolamine (MEA;$H_2NCH_2CH_2OH$) solution at room temperature. The molar ratio of MEA to zinc acetate was kept at 1.0. The resulting solution was stirred at 50 °C to obtain a clear homogeneous solution. Subsequently, manganese acetate tetrahydrate [$Mn(CH_3COO)4H_2O$] was added to the solution and stirred at 50 °C for 2 hr. Mn concentration was varied to 1, 3, 5, 7. 9 mol % with respect to Zn. The $Zn_{1-x}Mn_xO$ films were deposited by spin coating on quartz substrates (3000 rpm for 20 s). The films were dried at 300 °C for 10 min in air ambient to eliminate the solvent and organic residue. The same spin coating procedures were repeated five times. Finally, the films were post annealed at 1000, 1050, 1100, and 1200 °C for 3 h in air ambient so as to crystallize phosphor films. The crystallinity of obtained films was identified by X-ray diffraction (XRD) analysis using a Rigaku D/MAX 2500 with Cu Kα radiation. The cross-sectional images and surface morphologies were obtained by conventional scanning electron

microscopy (FE-SEM, JSM-6700F). The photoluminescence (PL) was measured in the transmission mode at room temperature using a 254 nm lamp (Vilber Lourmat VL-6 LC, 12 W) as the excitation source and a PR-650 SpectraScan spectroradiometer as the detector. The photoluminescence excitation (PLE) spectrum and decay curves were obtained using a Hitachi F4500 fluorescence spectrometer. Optical transmittance was measured using a UV-visible spectrometer (Hitachi U3000). To compare PL brightness between our film and a commercial powder phosphor, the same quantity of powder phosphor as the film (3 mg/cm^2) was used for screen printing.

4.2. $Zn_2SiO_4:Mn^{2+}$ PHOSPHOR SHELL

Manganese doped zinc silicate ($Zn_2SiO_4:Mn^{2+}$) phosphor layer on SiO_2 powder were prepared following procedure. Starting materials were ZnO (Ardrich), MnO (Ardrich), and SiO_2 powder (100~200 μm, Ardrich). Blended raw materials were annealed at 1150℃ for 7hrs in sealed vacuum (10^{-2} Torr) quartz tube. For complete reaction of ZnO, MnO and SiO_2 powder on SiO_2 powder surface, mol ratio of SiO_2 to ZnO was fixed at 2 mole %. Mn concentration was varied to 1, 3, 5, 7, 9 mol % with respect to Zn. The crystallinity of obtained phosphor films were identified by

X-ray diffraction (XRD) analysis using a Rigaku D/MAX 2500 with Cu Kα radiation. The cross-sectional images and surface morphology were obtained by conventional scanning electron microscopy (FE-SEM, JSM-6700F). The photoluminescence (PL), photoluminescence exitation (PLE), and decay curves were obtained using a Hitachi F4500 fluorescence spectrometer. Electron spin resonance (ESR) spectra were recorded at room temperature using a JEOL-JES PX2300 ESR spectrometer operating in the X-band frequency (9.4GHz)

4.3. $BaSi_2O_5:Eu^{2+}$ FILM PHOSPHOR

0.5 M sol-gel solution of $Ba_{1-x}Eu_xO$ was prepared for spin coating using the following procedure. Barium acetate [$Ba(CH_3COO)_2$] was dissolved in 2-methoxyethanol and acetic acid solution at 60 ℃. The solution was stirred at 60 °C to obtain a clear homogeneous solution. Subsequently, europium acetatehydrate [$Eu(CH_3COO)H_2O$] was added to the solution and stirred at 60 °C for 2 hrs. Eu concentration was varied to 1, 3, 5, 7, 9, 11, 13, 15 mol % with respect to Zn. The $Ba_{1-x}Eu_xO$ thin-films were deposited by spin coating on quartz substrates (3000 rpm for 20 s). The films were dried at 300 °C for 10 min in air ambient to eliminate the solvent and organic residue. The same spin coating

procedures were repeated 10 times. Finally, the films were annealed at 1000, 1050, 1100, 1150 °C for 5hrs and at 1100 °C for 1, 2, 5, 7 hrs in H_2 (5 %) /N_2 (95 %) atmosphere. The crystallinity of obtained films were identified by X-ray diffraction (XRD) analysis using a Rigaku D/MAX 2500 with Cu Kα radiation. The cross-sectional images and surface morphologies were obtained by conventional scanning electron microscopy (FE-SEM, JSM-6700F). The photoluminescence (PL) and photoluminescence excitation (PLE) spectra were obtained using PR-650 and Hitachi F4500 fluorescence spectrometer. Optical transmittance was measured using a UV-visible spectrometer (Hitachi U3000). The vacuum ultraviolet (VUV) spectrum obtained under vacuum ultraviolet (146 nm) by deuterium lamp.

5. RESULTS AND DISCUSSION

5.1. $Zn_2SiO_4:Mn^{2+}$ FILM PHOSPHOR

Figure 11 shows formation procedure of $Zn_2SiO_4:Mn^{2+}$ film phosphor. Figure 12 shows cross-section SEM images as a function of annealing temperature.

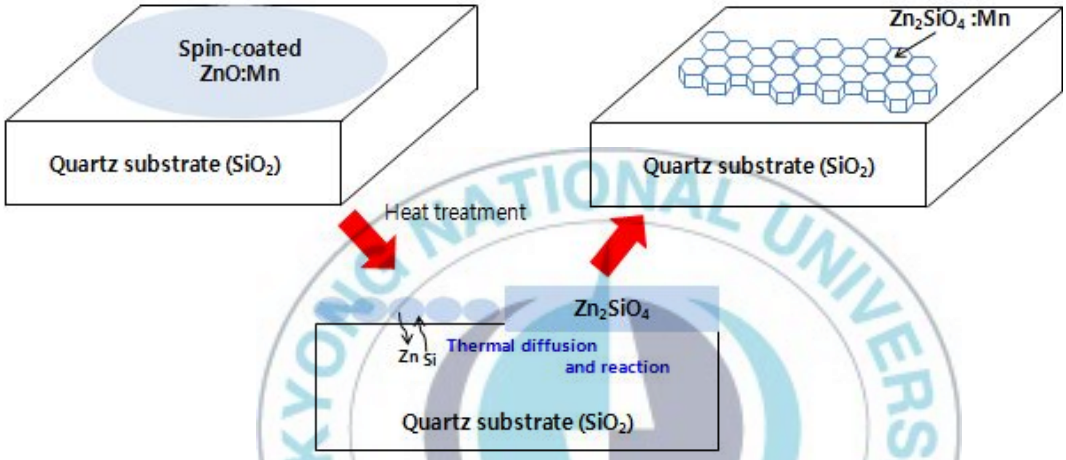

Figure 11. Schematic of formation procedure of $Zn_2SiO_4:Mn^{2+}$ film phosphor.

Figure 12(a) shows that spin-coated ZnO:Mn film has particle size of 50 nm and small particles stack up from quartz substrate to about thickness of 800 nm with a clear interface between the quartz substrate and the ZnO film. Its shape shows coarse-grained and large particle due to agglomeration of small particles through dry process for elimination of organic residual

after spin-coating. After annealing, dense and non-porous $Zn_2SiO_4:Mn^{2+}$ film was formed with 1000 nm-thickness, which is caused by thermal-diffusion reaction between spin-coated ZnO:Mn film and SiO_2 of quartz substrate. The interface of the formed $Zn_2SiO_4:Mn^{2+}$ film and the quartz substrate shows superior adhesion as seen in figure 12(d). With increasing annealing temperature, thickness of $Zn_2SiO_4:Mn^{2+}$ film slightly increases and the film becomes free of pores or grain boundaries, its interface becomes less distinct, and the average thickness increases up to 1000 nm for the film annealed at 1100 °C shown in figure 12(d). It should be noted that the thickness of the film annealed at 1200 °C [figure 12(e)] is markedly reduced, which can be explained by a pronounced sublimation of ZnO at a critical temperature of 1200 °C[49].

Figure 13 shows the top-view SEM images of films with increasing annealing temperature. The as-grown film (a) consists of ellipsoidal particles about 100 nm in size. As the annealing temperature increases, the surface appears gradually denser while the grains grow from 100 up to 2000 nm for the film (e) annealed at 1200 °C.

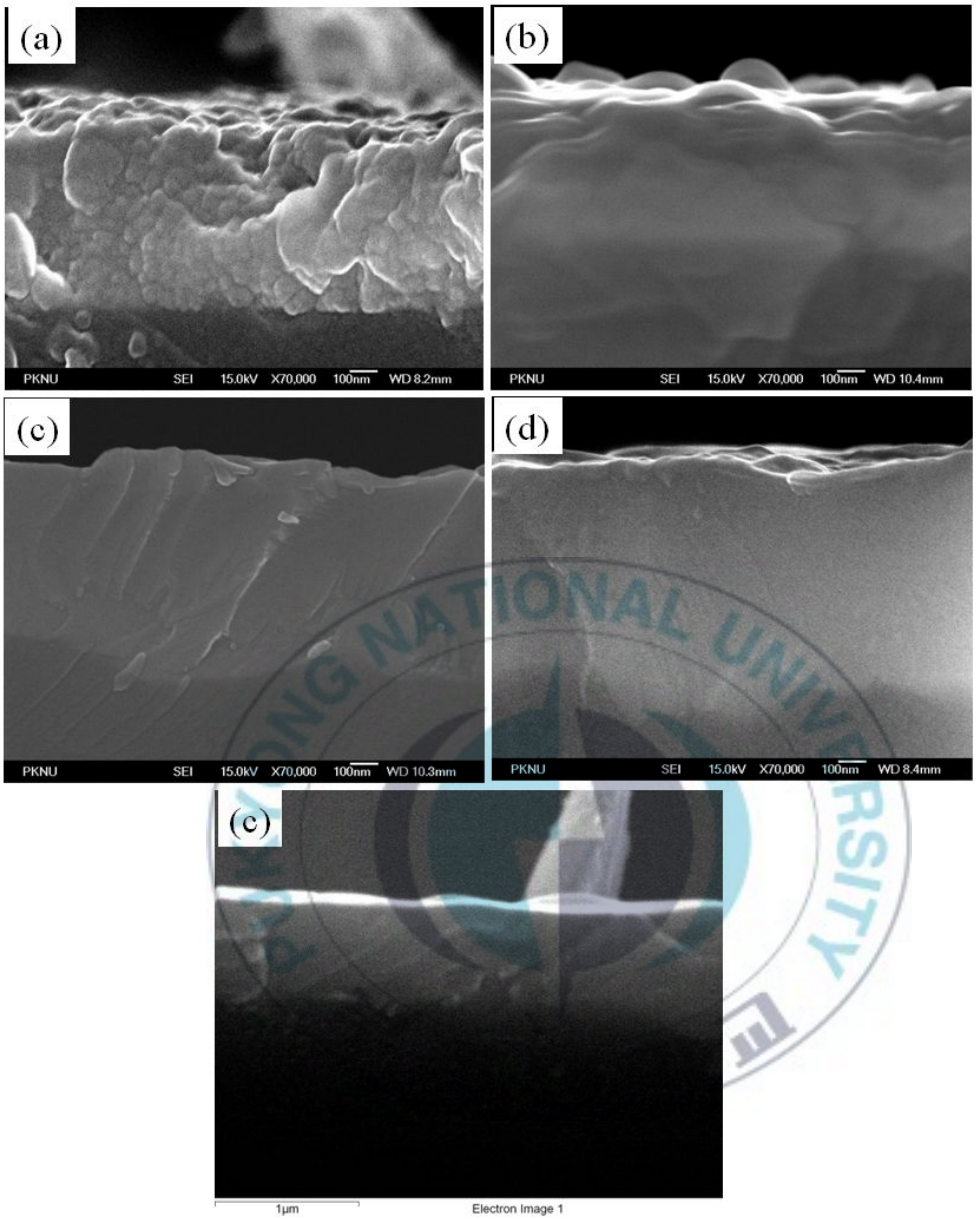

Figure 12. Cross-section SEM images of $Zn_2SiO_4:Mn^{2+}$ film phosphoras a function of annealing temperature: (a) as-grown, (b) 1000 ℃, (c) 1050 ℃, (d) 1100 ℃, (e) 1200 ℃.

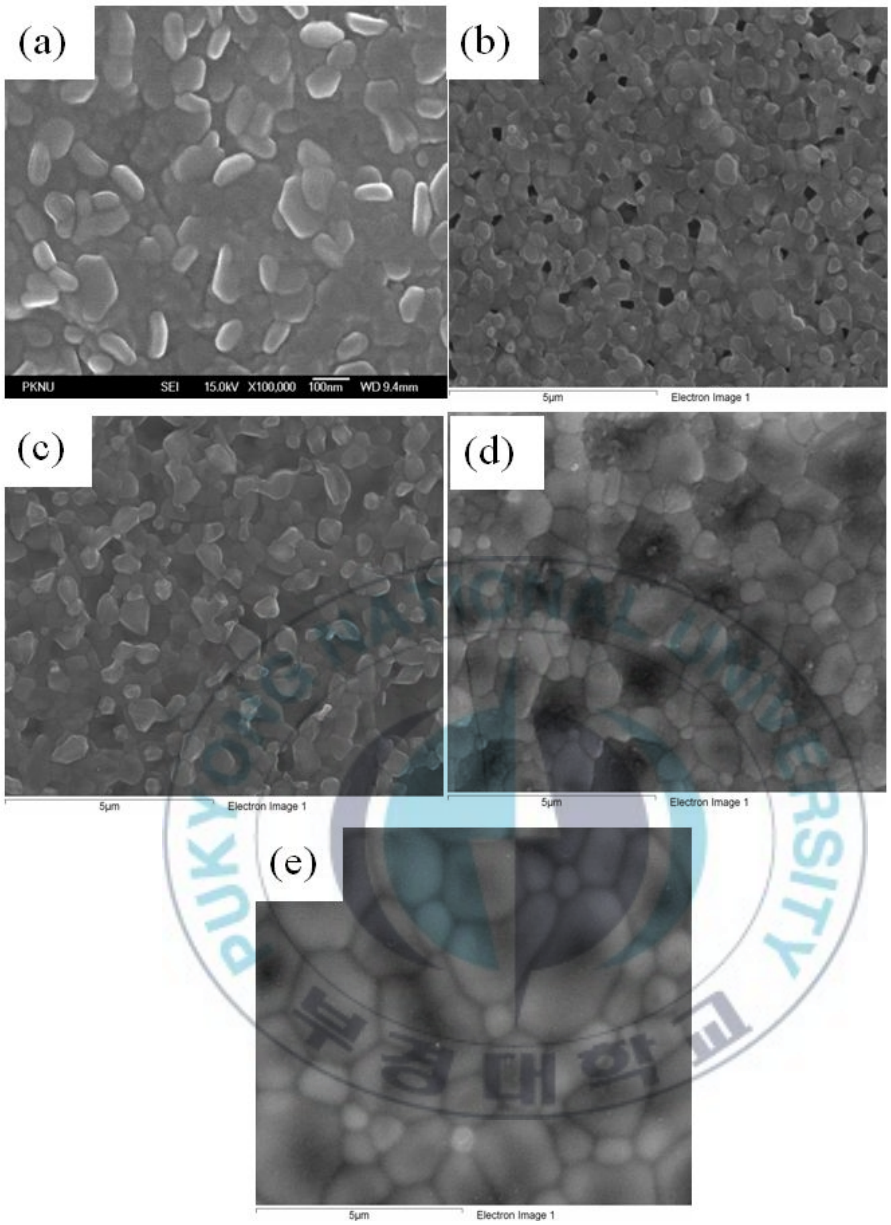

Figure 13. Top-view SEM images of $Zn_2SiO_4:Mn^{2+}$ film phosphor as a function of annealing temperature: (a) as-grown, (b) 1000 ℃, (c) 1050 ℃, (d) 1100 ℃, (e) 1200 ℃.

Figure 14 shows the XRD patterns of the samples annealed at different temperatures.

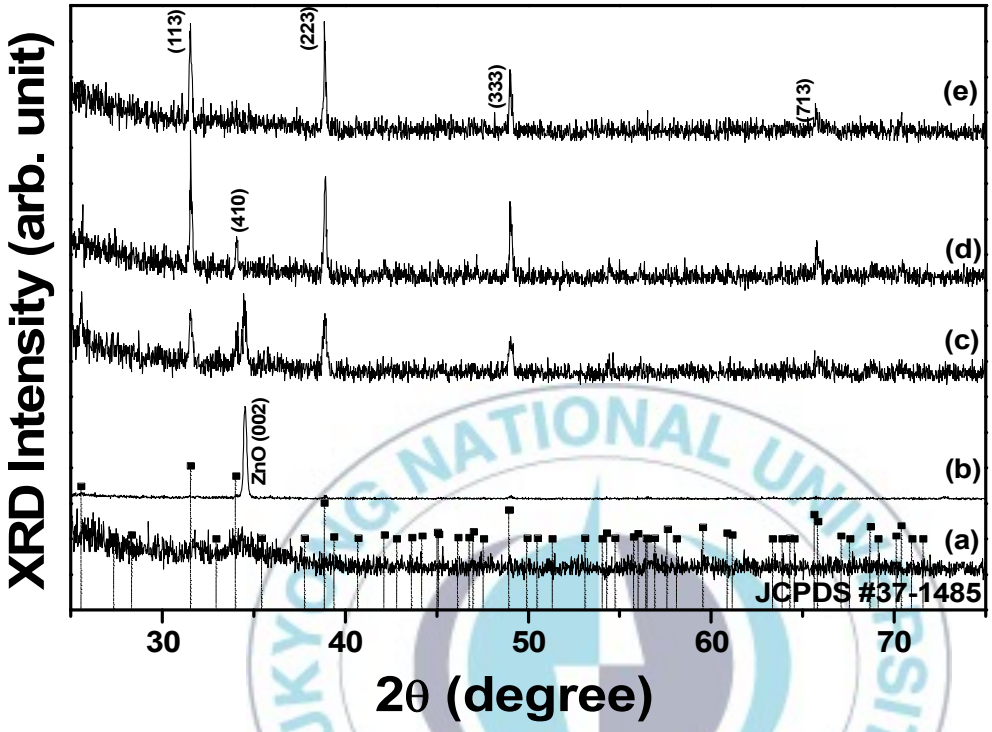

Figure 14. XRD patterns of $Zn_2SiO_4:Mn^{2+}$ film phosphor as a function of annealing temperature: (a) as-grown, (b) 1000 ℃, (c) 1050 ℃, (d) 1100 ℃, (e) 1200 ℃.

No diffraction peak is found in the as-grown film (a), indicating that the spin-coated ZnO film on quartz glass is amorphous. In figure 14(b), for the film annealed at 1000 ℃, only a single diffraction peak is observed at 2θ = 34.5 °, which corresponds to the (002) plane of the hexagonal ZnO crystal structure [Joint

Committee on Powder Diffraction Standards (JCPDS) 79-0205]. Three dominant diffraction peaks are observed as the annealing temperature increases to 1050 °C, as shown in figure 14(c). These three peaks are found at 2θ = 31.5, 38.8, and 48.9 °, corresponding to the (113), (223), and (333) planes of the Zn_2SiO_4 crystal in the hexagonal structure vertically along the *c*-axis with rhombohedral symmetry (JCPDS 37-1485). As the annealing temperature increases, ZnO-related (002) peak intensity significantly decreases, whereas Zn_2SiO_4-related peak intensity gradually increases. Sample (c) annealed at 1050 °C contains both phases of ZnO and Zn_2SiO_4, while samples (d) and (e) annealed above 1050 °C consist of a single phase of Zn_2SiO_4. This shows that a higher temperature is more effective in thermally diffusing the as-grown ZnO:Mn and quartz-based SiO_2, and in inducing a Zn_2SiO_4:Mn^{2+} crystallization. It is noted that Zn_2SiO_4:Mn^{2+} crystals exhibit (113)-, (223)-, and (333)-textured crystallizations, even though several polycrystals are usually expected to form on amorphous quartz. Here, we define a parameter to describe the degree of (113) texture in the films given by

$$f = \frac{I(113)}{I(113)+I(410)}$$

here I(113) is the (113) peak intensity, and I(410) is the strongest (410) peak intensity in JCPDS file # 37-1485. For polycrystalline powders based on JCPDS file # 37-1485, I(113) = 1.55 × I(410) and f= 0.53. For a completely (113)-textured Zn_2SiO_4 film, I(410) = 0 and f = 1. Normally, 0.53 < f < 1 represents a partially (113)-textured film. For higher annealing temperatures, the Zn_2SiO_4 films become more textured, and f approaches unity; f = 0.66 at 1050 ℃, f = 0.79 at 1100 ℃, and f = 0.92 at 1200 ℃. Amorphous quartz consists of a statistical distribution of hexagonal rings formed by SiO_2 tetrahedra and oxygen atoms in which only a few of such rings are regular[50]. It is well known that the incorporation of metallic elements such as Zn and Mn into amorphous quartz promotes the crystallization into a periodic distribution of hexagonal rings[51]. At lower temperatures, the interdiffusion of Zn and Si ions causes the phase transition from both amorphous ZnO and SiO_2 hosts to a common hexagonal structure. With the prolongation of thermal diffusion, Zn and Si ions can replace what so that Zn_2SiO_4:Mn^{2+} crystals are formed along the hexagonal directions where the misfit stress between hexagonal ZnO and hexagonal-like SiO_2 is lower than those along other directions.

Figure 15 shows the concentration depth profiles of Zn and

Si in the thickest sample (annealed at 1100 °C) measured by energy dispersive X-ray spectroscopy (EDX) during SEM.

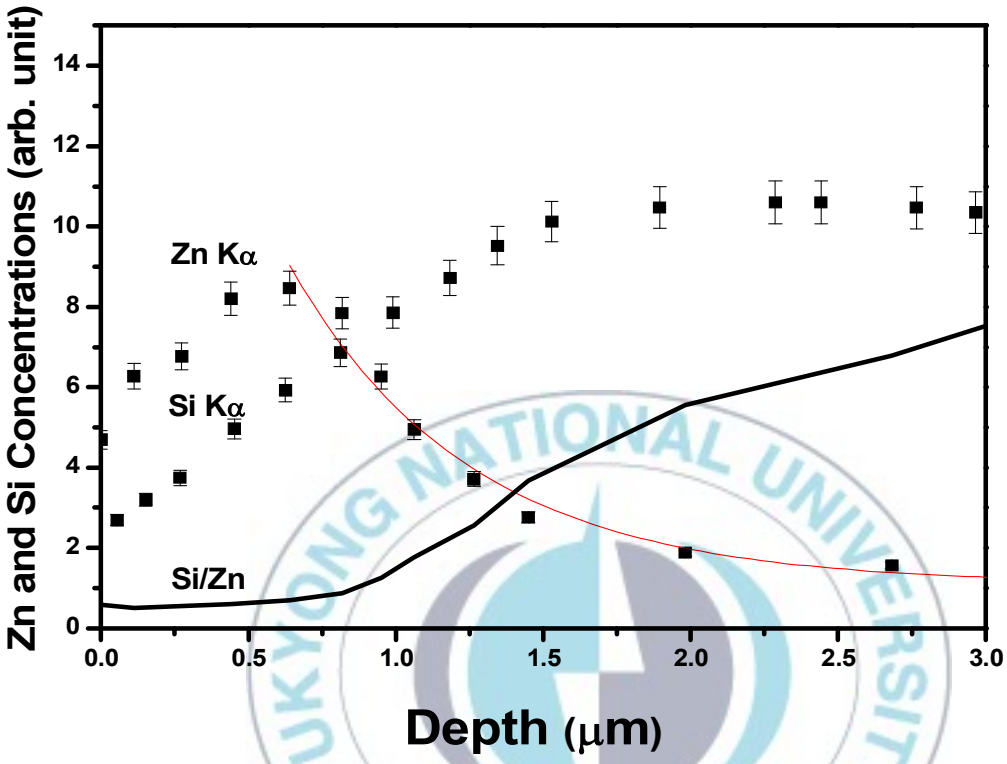

Figure 15. Concentration depth profiles of Zn and Si in $Zn_2SiO_4:Mn^{2+}$ film phosphor.

Within the substrate, Si concentration is found to increase away with distance from the film/substrate interface whereas Zn content decreases, indicating the continuous grading of the interface chemical composition. This further confirms the mechanism of the

thermal interdiffusion of Zn and Si ions. Furthermore, the interdiffused Zn ions consume only a stoichiometric ratio (2:1) of SiO_2 so as to achieve only stoichiometric Zn_2SiO_4:Mn^{2+} crystals embedded the unreacted SiO_2 host. The calculated Si/Zn profile is indicative of the amount of unreacted SiO_2 surrounding Zn_2SiO_4 crystals. Within the resulting Zn_2SiO_4:Mn^{2+} region, the Zn concentration peaks near the film/substrate interface with a wide spread across the 1000 nm thickness.

Figure 16 shows the transmittance spectrum of the 1100 °C-annealed sample in the visible wavelength range. Transmittances ranging from 50% at a wavelength of 450nm to 70% at a wavelength 620 nm were achieved. Generally, the transparency of a ceramicis limited by light scattering from grains boundaries or pores, and by back optical reflection at the film-substrate interface[52]. The textured grain growth in our films is expected to result in a lower number of grain boundaries, and hence less scattering or absorption at such grain boundaries. Furthermore, the continuous grading of the interface chemical composition of our films as shown in figure 15 is expected to improve the refractive index matching between the Zn_2SiO_4:Mn^{2+} phosphor film and the substrate at the interface, thus further reducing the degree of back optical reflection.

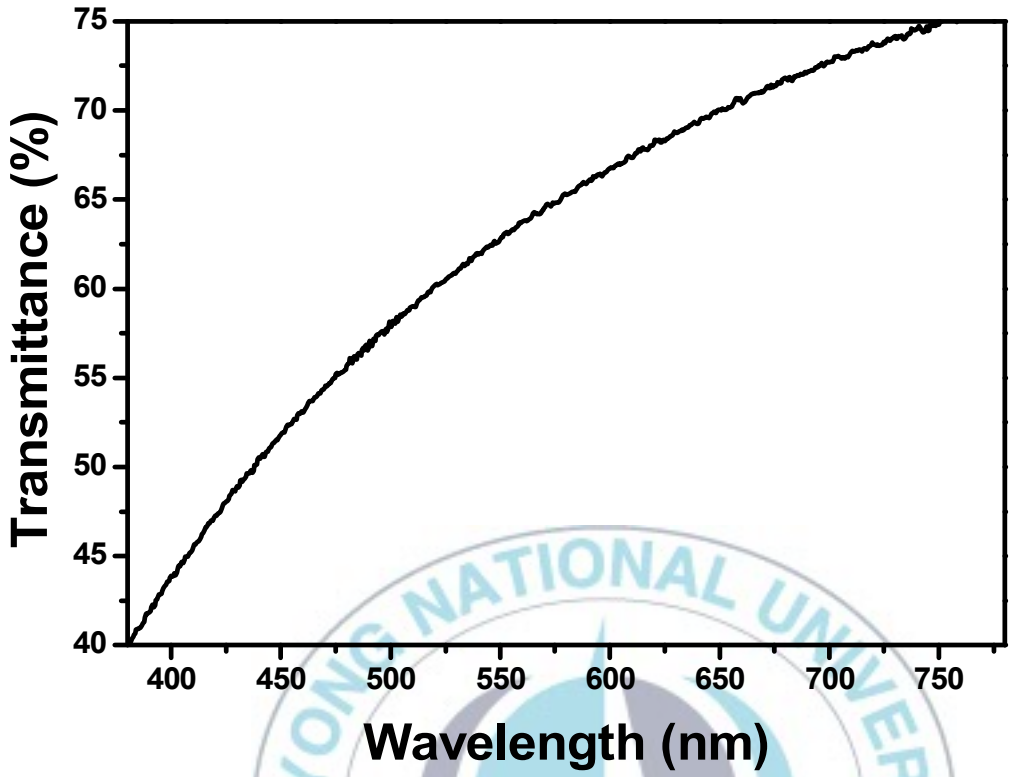

Figure 16. Transmittance spectrum of $Zn_2SiO_4:Mn^{2+}$ film phosphor.

Figure 17 shows the PL decay curves of the samples annealed at various temperatures. $Zn_2SiO_4:Mn^{2+}$ phosphor is known to have a relatively slow decay on the order of milliseconds owing to the spin-forbidden $^4T_1-^6A_1$ transition of Mn^{2+} ions. There are two possible PL decay processes: a slow one arising from isolated Mn^{2+} ions and a fast one from Mn^{2+} pairs, depending on both Mn^{2+} concentration and annealing temperature.

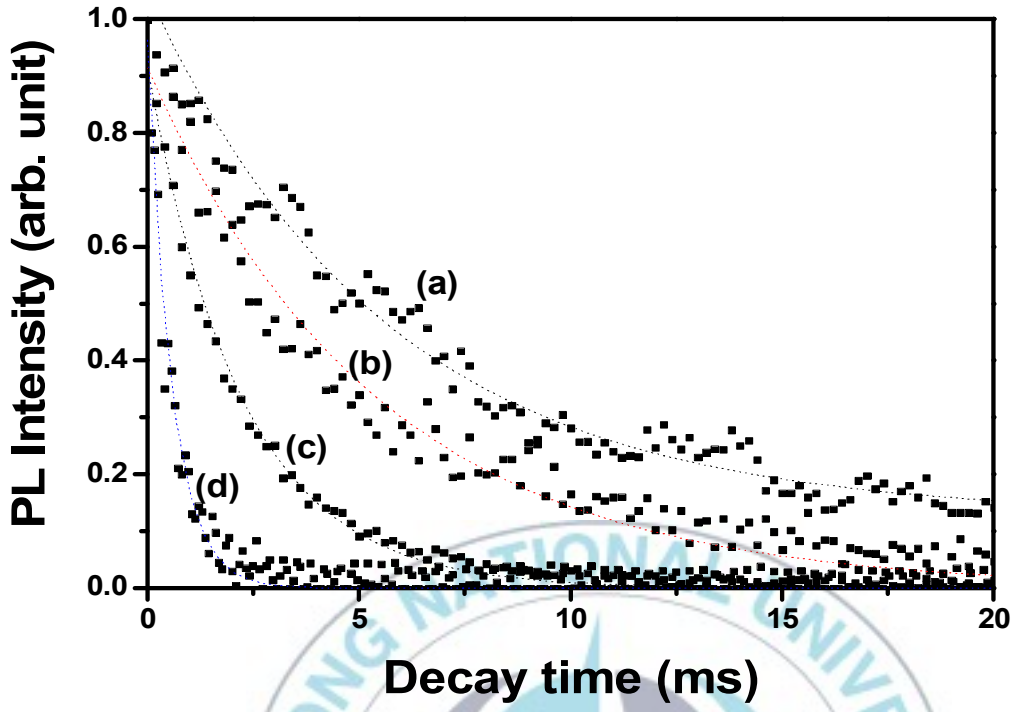

Figure 17. Decay curves of $Zn_2SiO_4:Mn^{2+}$ film phosphor as a function of annealing temperature: (a) 1000 ℃, (b) 1050 ℃, (c) 1100 ℃, (d) 1200 ℃.

A faster decay is expected with increasing Mn^{2+} concentration owing to the pairing of Mn^{2+} ions, while annealing at higher temperatures can reduce the probability of Mn^{2+} pair formation as a result of the higher rate of thermal diffusion[53,54]. Therefore, the PL decay is generally expected to be slower for higher temperature annealed sample. However, our samples show the opposite trend as measured decay time actually decreases: from $\tau_{10\%}$ = 11.5 ms for the 1050 °C-annealed sample to 4.4 ms for the 1100

°C-annealed sample, and to 1.3 ms for the 1200 °C-annealed sample. Importantly, the decay time of the brightest sample (4.4 ms, annealed at 1100 °C) was much shorter than that of powder phosphor ($\tau_{10\%}$ = 13.3 ms) that was doped with Mn^{2+} to the same concentration to avoid any effect due to Mn^{2+} concentration. The 4.4 ms decay time is smaller than the 12.5 ms decay time obtained from the other films deposited by pulse-laser deposition and then annealed at the same temperature[55]. The shortening of decay time in our samples can be explained in terms of the anisotropic textured crystal structure. It is reported that decay time is a function of the parity selection rule, which is strongly dependent on the local structure environment[1,14]. The symmetry of Mn^{2+} ions in our textured phosphor film may be lower than the regular tetrahedral symmetry of Mn^{2+} ions in a polycrystalline host lattice; therefore, it may induce an asymmetric crystal on Mn^{2+} ions that relaxes the spin-selection rule and enhances the transition probability, thus decreasing decay time. This interpretation is supported by the strong correlation between the degree of texture, *f,* and the inverse of decay time, τ^{-1}, as a function of annealing temperature, as shown in the figure 18: as annealing temperature increases, τ^{-1} consistently increases together with *f*.

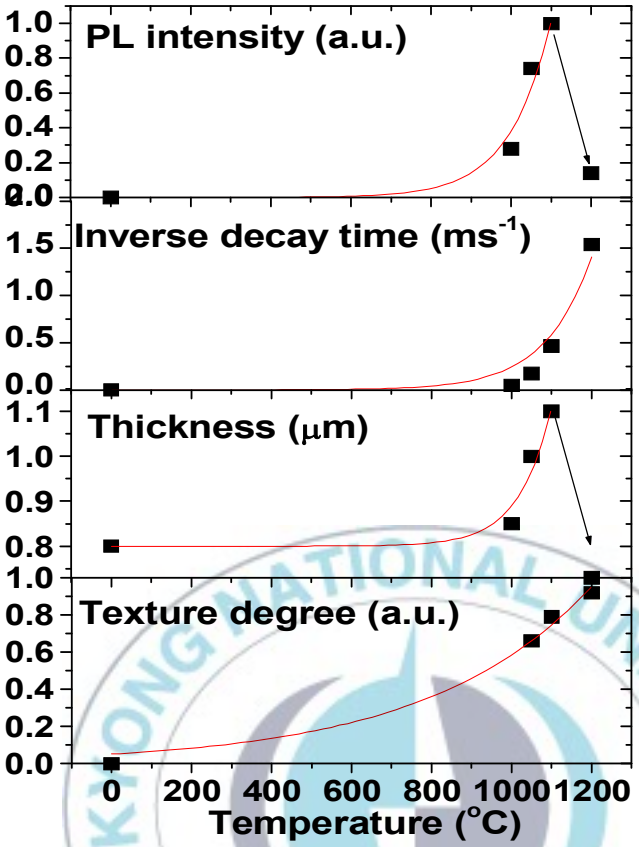

Figure 18. PL intensity, inverse decay time (τ^{-1}), thickness, and texture degree (f) of $Zn_2SiO_4:Mn^{2+}$ film phosphor as a function of annealing temperature.

Figure 19 shows the PL spectra excited at 254 nm from the samples with increasing annealing temperature, and the PLE spectrum monitored at 526 nm for the 1100 °C-annealed sample shown in figure 20.

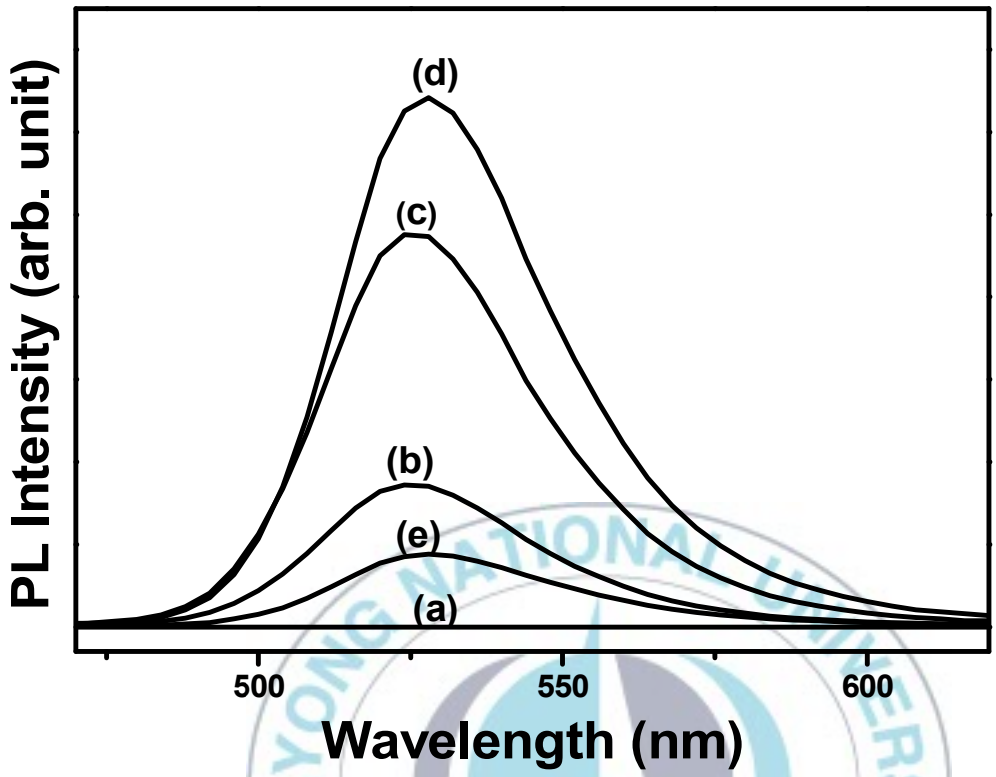

Figure 19. PL spectra of $Zn_2SiO_4:Mn^{2+}$ film phosphor as a function of annealing temperature: (a) as-grown (b) 1000 ℃, (c) 1050 ℃, (d) 1100 ℃, (e) 1200 ℃.

The PL and PLE spectra show typical characteristics of Mn^{2+} ions in the Zn_2SiO_4 host lattice. As annealing temperature increases, the PL emission is significantly enhanced and reaches a maximum at 1100 °C before rapidly decreasing for the sample annealed at 1200 °C. In general, the PL intensity of phosphor films is determined by their surface roughness: the higher the surface

roughness, the higher the out coupling efficiency and PL intensity. However, the theory of this surface effect of PL intensity is limited to the case of surface roughness lower than 200 nm[6]. Therefore, it can not explain the PL enhancement of our films, which have micron-sized grains.

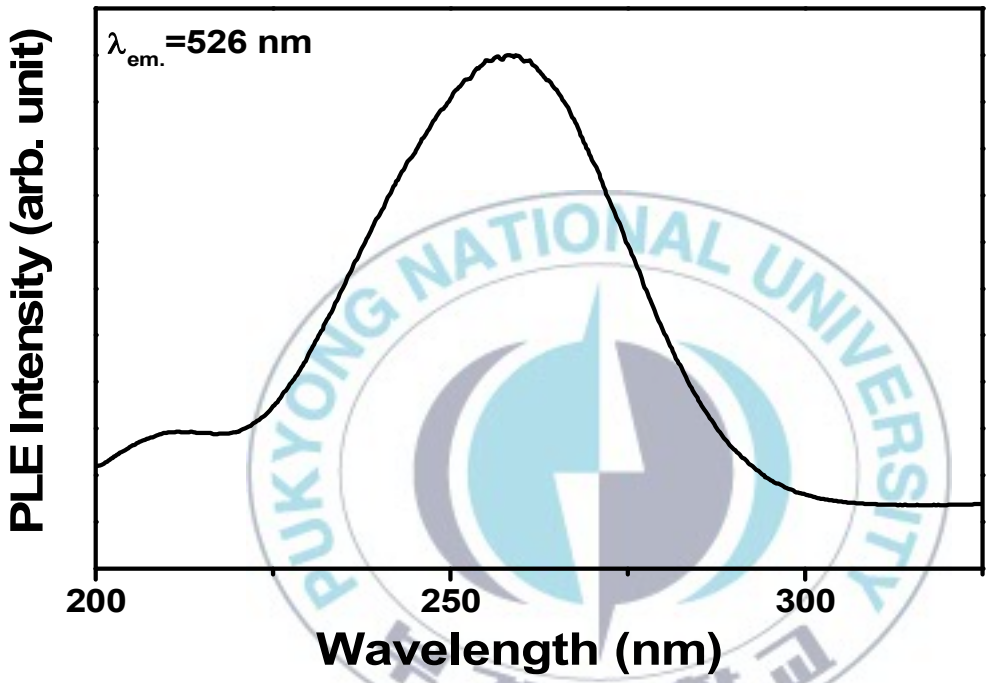

Figure 20. PLE spectrum of $Zn_2SiO_4:Mn^{2+}$ film phosphor annealed at 1100 ℃.

In our films, we can explain the behaviour of the PL intensity changes in terms of the changes in texture degree, decay time, and film thickness as seen in figure 18. A higher annealing

temperature improves the crystallinity as well as the texture degree of the films. This enhanced texture degree changes the local environment of Mn^{2+} ions, resulting in a shorter decay time, i.e., an increased transition probability. The observed PL intensity changes are thus consistent with the changes in inverse decay time and texture degree. For the sample annealed at 1200 °C, a pronounced sublimation at the top of the ZnO film occurs, leading to a marked reduction in the amount of Zn_2SiO_4:Mn^{2+} crystals formed. As a result in the case of sample annealed at 1200 °C, although changes in the texture degree and inverse decay time are expected to enhance PL emission, such sublimation has a stronger adverse effect on PL intensity. This high vaporization of ZnO can be prevented by a appropriate high-pressure ambient gas, and thus the decreases in thickness and PL intensity can be limited. However this would be the subject of a separate study.

Figure 21 shows XRD patterns of (223) crystal plane in Zn_2SiO_4:Mn^{2+} film as a function of Mn concentration. Peak position of (223) plane shift to low angle as increasing Mn^{2+} concentration. It is due to the lattice expansion caused by substitution of slightly large Mn^{2+}(0.80Å) ions in small Zn^{2+}(0.74Å) site.

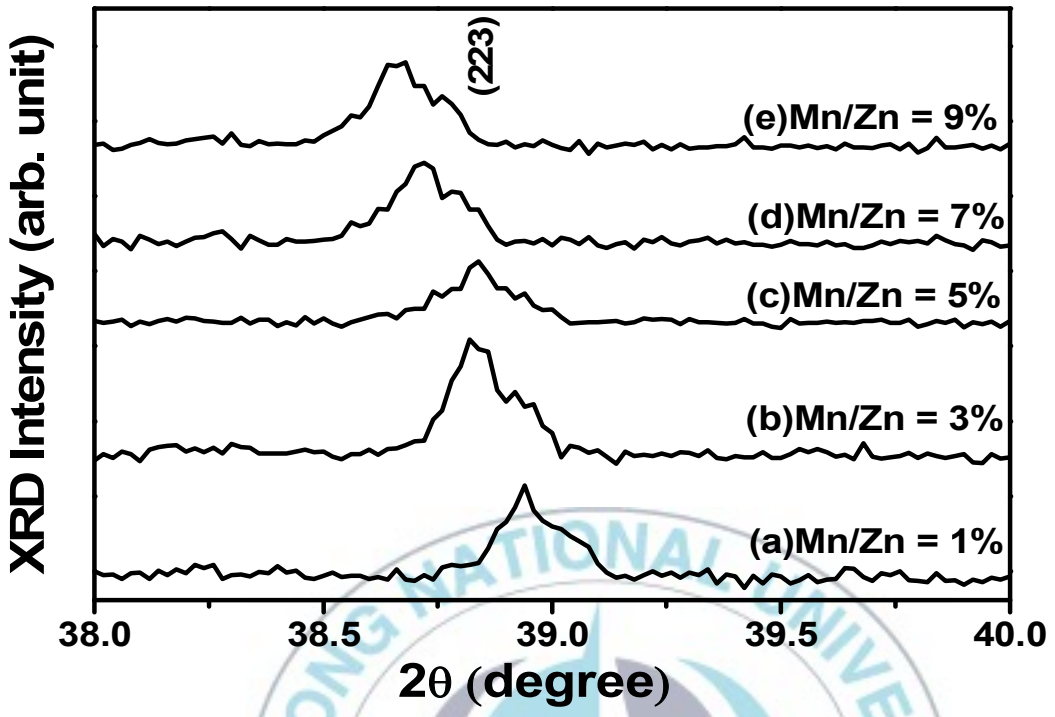

Figure 21. XRD patterns of (223) crystal plane of $Zn_2SiO_4:Mn^{2+}$ film phosphor as a function of Mn^{2+} concentration.

Figure 22 shows PL spectra of $Zn_2SiO_4:Mn^{2+}$ film phosphor compared to commercial powder phosphor excited by 254 nm with increasing Mn^{2+} concentration. Maximum PL intensity is appeared at 5 mol % Mn^{2+} in $Zn_2SiO_4:Mn^{2+}$ film which shows 65 % brightness compared to commercial powder phosphor. And it shows green emission peaking at 526 nm due to atomic transition from $^4T_1$ to $^6A_1$ in d-orbital of Mn^{2+} ions. Concentration quenching starting

pointis 7 mol % Mn^{2+} and PL peak position shift from 519 nm to 526 nm with increasing Mn^{2+} concentration in Zn_2SiO_4:Mn^{2+} as seen in normalized PL spectra of figure 23.

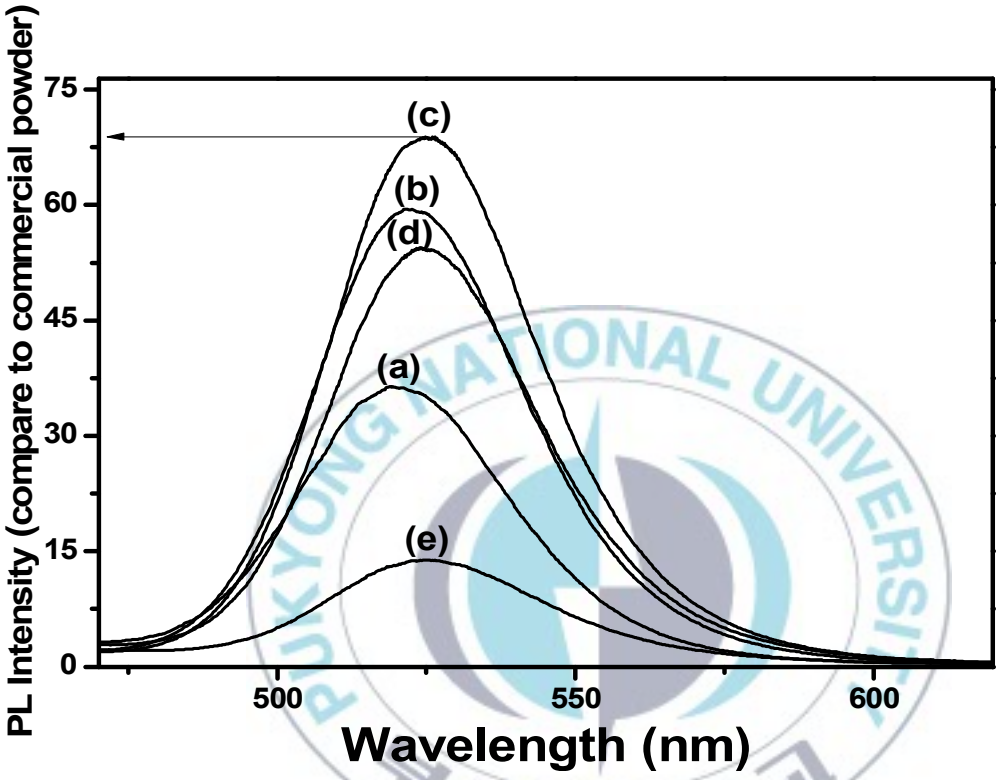

Figure 22. PL spectra of Zn_2SiO_4:Mn^{2+} film phosphor as a function Mn^{2+} concentration: (a) Mn/Zn = 1 %, (b) Mn/Zn = 3 %, (c) Mn/Zn = 5 %, (d) Mn/Zn = 7 %, (e) Mn/Zn = 9 %.

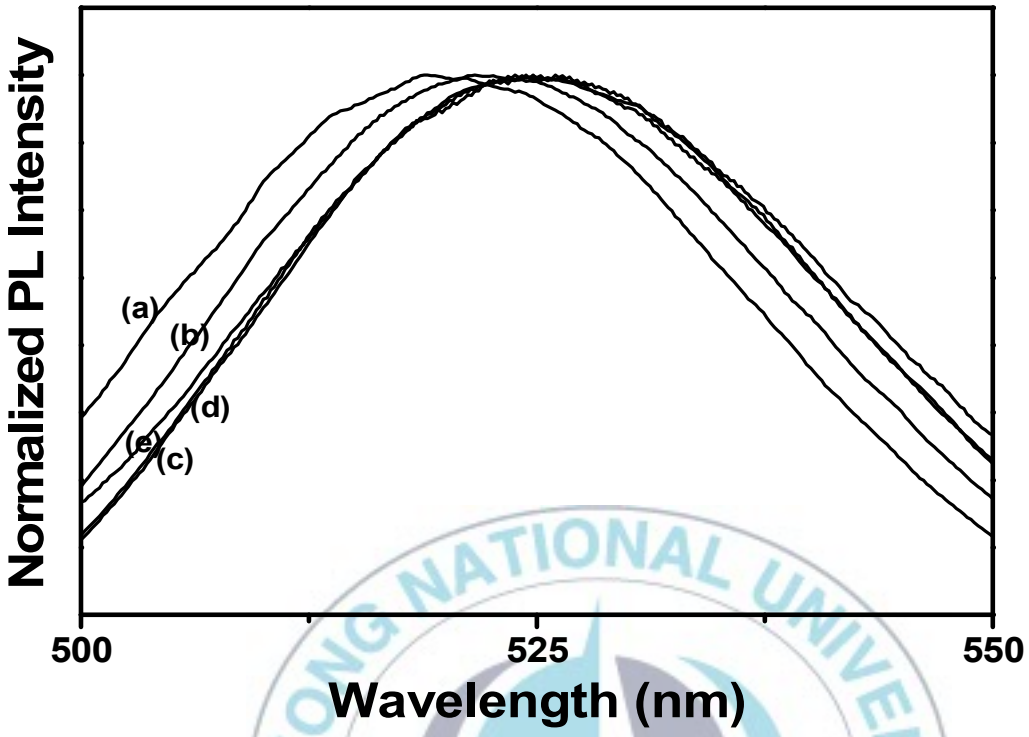

Figure 23. Normalized PL spectra of $Zn_2SiO_4:Mn^{2+}$ film phosphor as a function Mn^{2+} concentration: (a) Mn/Zn = 1 %, (b) Mn/Zn = 3 %, (c) Mn/Zn = 5 %, (d) Mn/Zn = 7 %, (e) Mn/Zn = 9 %.

We investigated the decay time of $Zn_2SiO_4:Mn^{2+}$ film as a function of Mn^{2+} concentration. Figure 24 shows decay curves on Mn^{2+} concentration in $Zn_2SiO_4:Mn^{2+}$. Decay time decreases from 20 ms to 0.5 ms with an increase in the Mn^{2+} concentration as seen in figure 24.

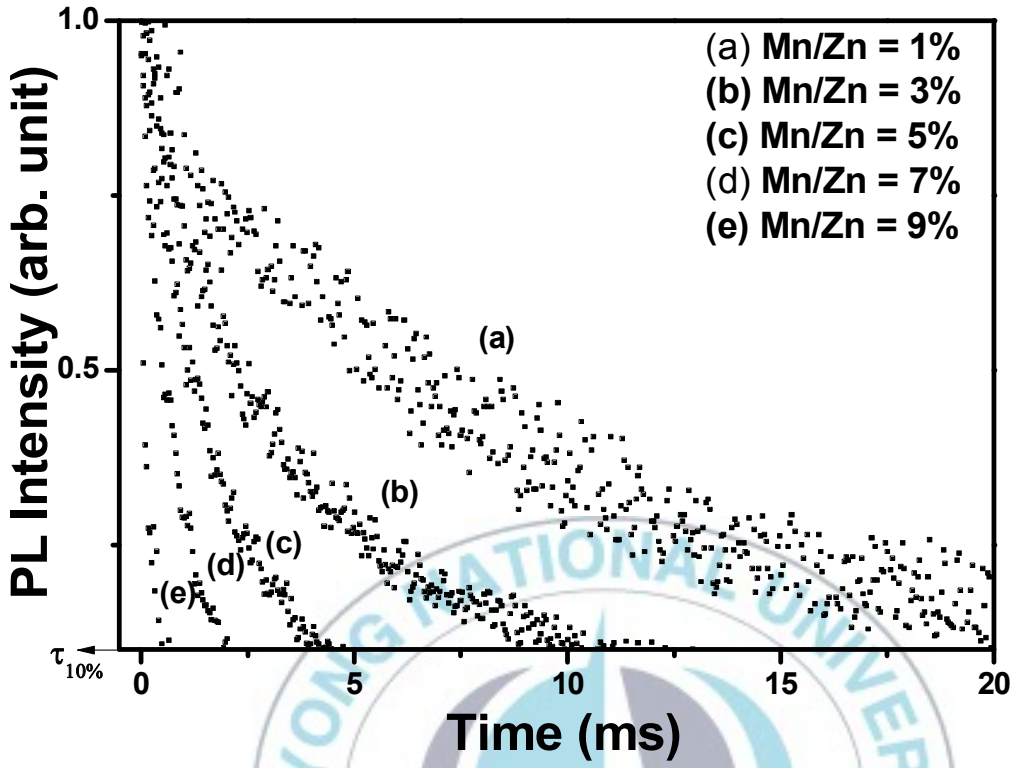

Figure 24. Decay curves of $Zn_2SiO_4:Mn^{2+}$ film phosphor as a function Mn^{2+} concentration: (a) Mn/Zn = 1 %, (b) Mn/Zn = 3 %, (c) Mn/Zn = 5 %, (d) Mn/Zn = 7 %, (e) Mn/Zn = 9 %.

These red-shift of emission peak and short decay time with increasing Mn^{2+} concentration have been explained that Mn-Mn exchange interaction or Mn-Mn pairing[40,44]. Generally, decay time of our film samples is short compared to powder phosphor reported by other researchers[44,56]. These behaviors can be explained by morphology and unique crystalline of formed

Zn_2SiO_4:Mn^{2+} film on quartz. Dense and closely packed shape (figure 12, 13) of our film in limited area can give stress to Mn^{2+} ions. This stress have directional properties caused by unique crystalline having some preferred crystal plane as seen in figure 14. In addition, as increasing the Mn^{2+} concentration large-size Mn^{2+} ions gradually expand the lattice size of Zn_2SiO_4 crystal when Zn^{2+} site substituted with Mn^{2+} ions. We assume that expansion of lattice size is processed to restore its original lattice condition, at this moment, give stress to Mn^{2+} ions that is self-induced stress of Mn^{2+} ions as seen in figure 25.

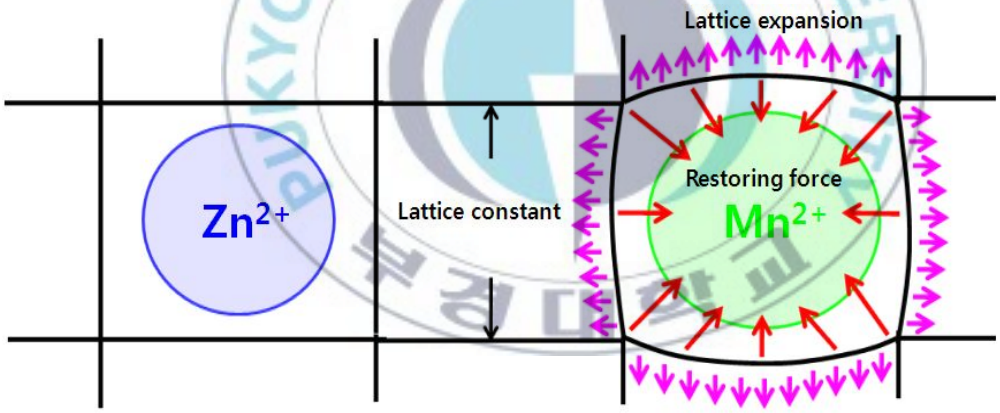

Figure 25. Schematic of position of Mn^{2+} in Zn_2SiO_4 crystal of Zn_2SiO_4:Mn^{2+} film phosphor.

This stress increases with increase of Mn^{2+} concentration in

$Zn_2SiO_4:Mn^{2+}$ film. Also, symmetry of the surrounding of Mn^{2+} ions is lower due to unique crystalline of our film. All these factors can influence the transition of Mn^{2+} ions in $Zn_2SiO_4:Mn^{2+}$ film. This give rise to short decay time and red shift of emission of Mn^{2+} ions with increasing Mn^{2+} ions concentration in $Zn_2SiO_4:Mn^{2+}$.

Figure 26 shows PL intensity of $Zn_2SiO_4:Mn^{2+}$ film phosphor excited by VUV (146 nm) with increasing the Mn concentration.

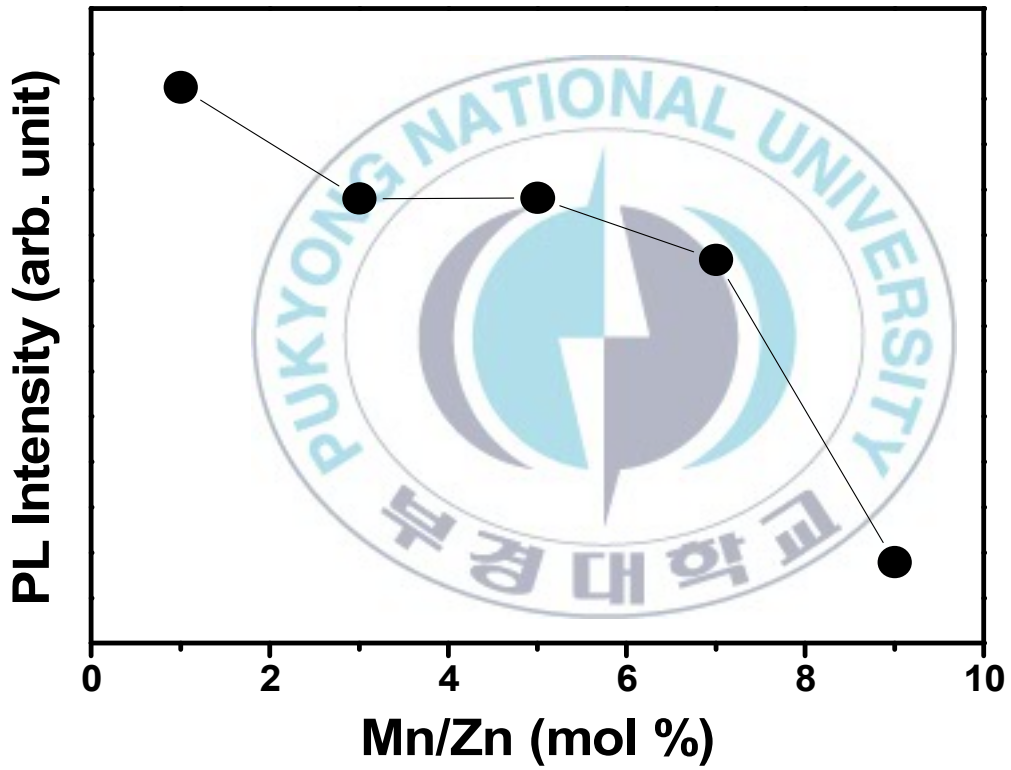

Figure 26. PL intensity $Zn_2SiO_4:Mn^{2+}$ film phosphor excited by 146 nm VUV.

PL intensity was decrease as increase of Mn^{2+} concentration. Difference of Mn^{2+} quenching concentration on excitation energy is considered by different energy transfer process[57]. Figure 27 shows VUV excitation spectrum.

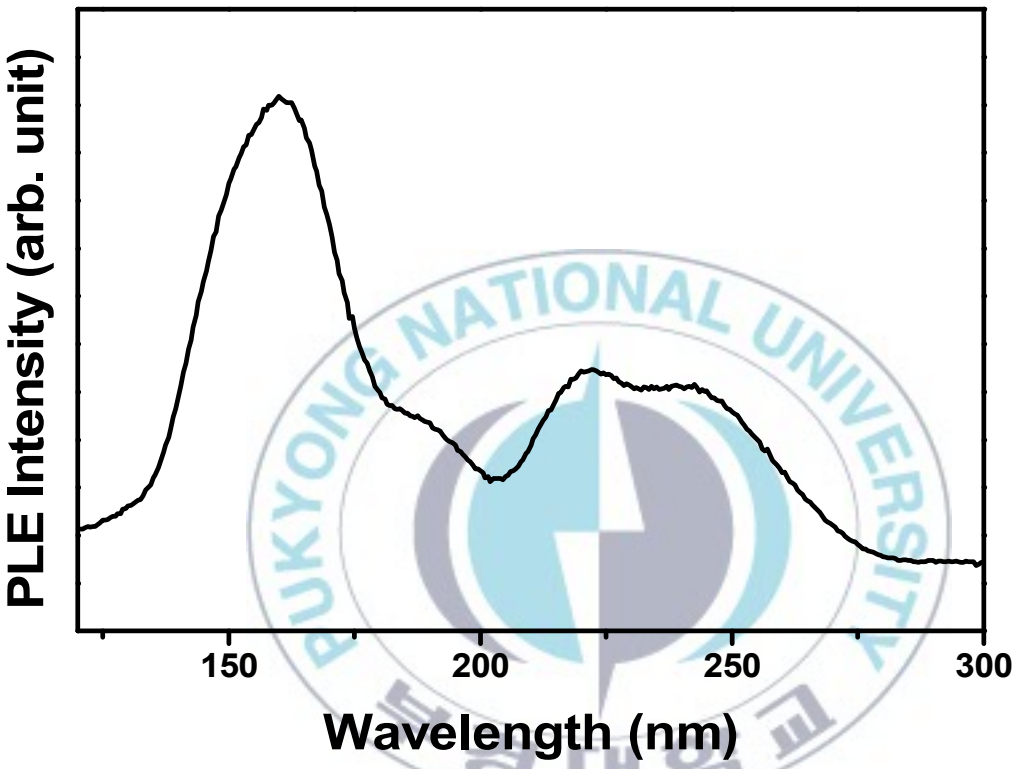

Figure 27. VUV excitation spectrum of Zn_2SiO_4:Mn^{2+} film phosphor.

This shows that our film sample effectively absorbed in VUV region from 132 nm to 190 nm related SiO_4 and ZnO_4 cluster and excitation band from 200nm to 275nm is due to the charge transfer

transition of Mn^{2+} in Zn_2SiO_4 host. Considering decay time of film sample, 5 mol %-Mn doped film sample was selected as best sample in order to compare commercial powder product under VUV. Its luminescence intensity was 40% brightness compared to that of commercial powder product shown in figure 28.

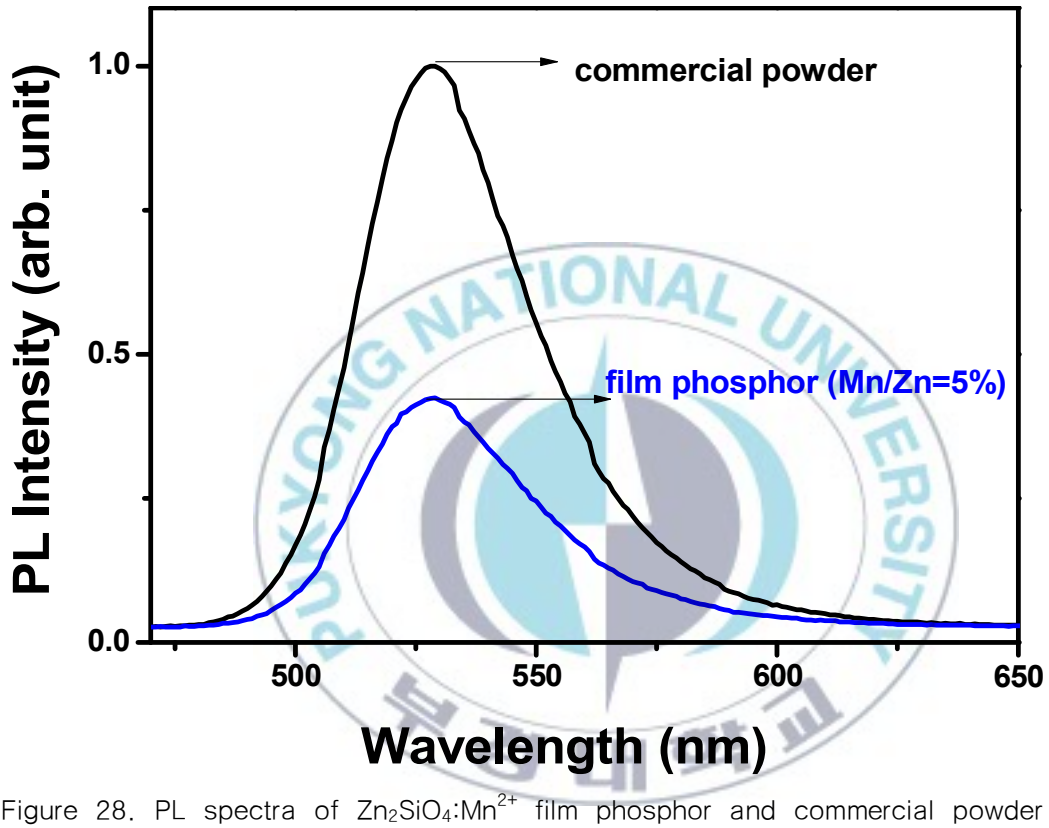

Figure 28. PL spectra of $Zn_2SiO_4:Mn^{2+}$ film phosphor and commercial powder phosphor excited by 146 nm VUV.

These excellent luminance properties can be explained by morphology and unique crystalline of our film samples. Dense and

closely packed shape of our film reduce luminescence killer such as pores, grain boundaries and effectively absorb excitation wavelength. In addition, directed crystalline reduce boundaries between grains. These factors affect optical properties of our film phosphor. Figure 29 shows photograph of our $Zn_2SiO_4:Mn^{2+}$ film phosphor grown on 1-inch quartz substrate under daylight lamp.

Figure 29. Photograph of $Zn_2SiO_4:Mn^{2+}$ film phosphor under day light lamp.

5.2. $Zn_2SiO_4:Mn^{2+}$ PHOSPHOR SHELL

Figure 30 shows top-view and cross-section scanning electron microscope (SEM) images of $Zn_2SiO_4:Mn^{2+}$ phosphor shell on surface of SiO_2 powder having 100 μm particle size.

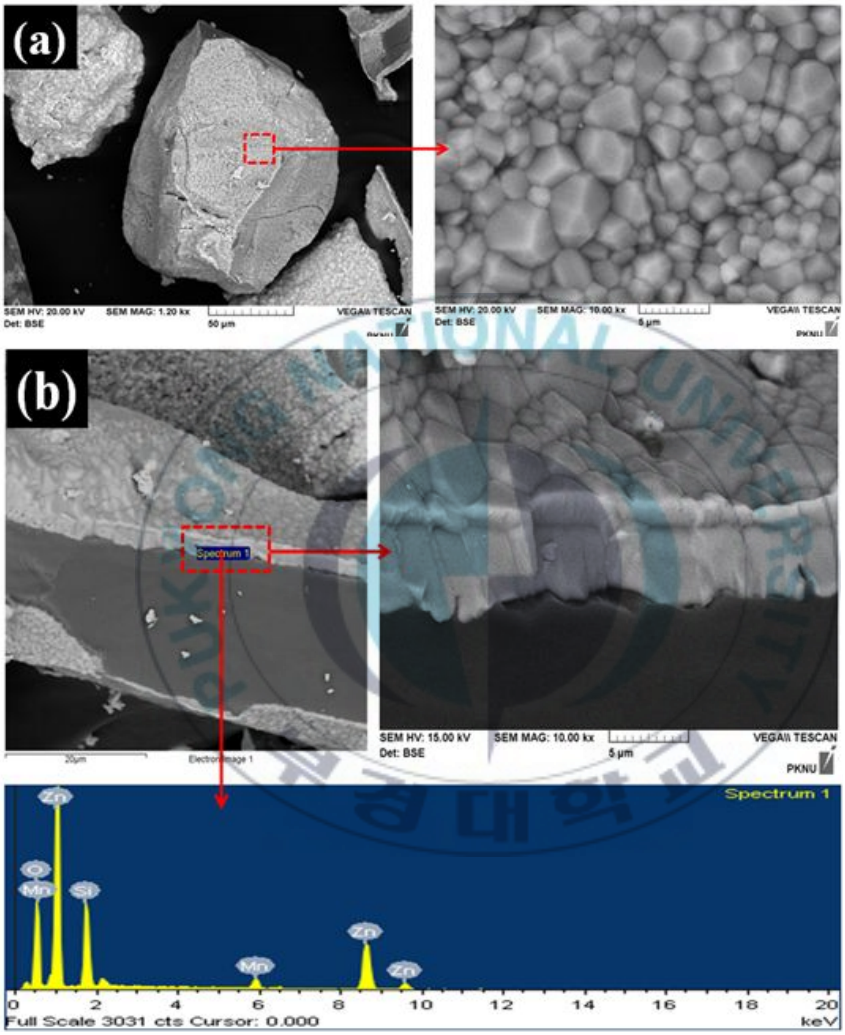

Figure 30. (a) Top-view and (b) cross-section SEM images of $Zn_2SiO_4:Mn^{2+}$ phosphor shell on SiO_2 powder and EDS spectrum.

$Zn_2SiO_4:Mn^{2+}$ phosphor shell has 2~5 μm size and it has thickness of 5 μm with densely packed shape. $Zn_2SiO_4:Mn^{2+}$ phosphor shell formed to limited area of SiO_2 powder shape.

Figure 31 shows XRD patterns of SiO_2 powder and $Zn_2SiO_4:Mn^{2+}$ phosphor shell on SiO_2 powder.

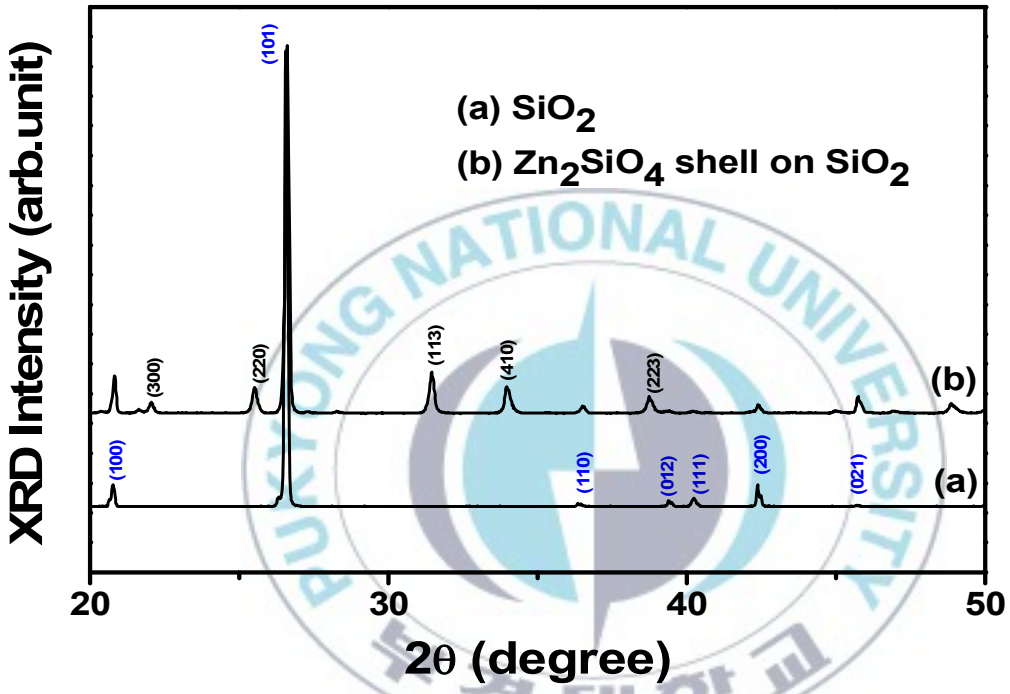

Figure 31. XRD patterns of (a) SiO_2 and (b) $Zn_2SiO_4:Mn^{2+}$ phosphor shell on SiO_2.

Diffraction peaks belong to hexagonal SiO_2 crystal and wellimite Zn_2SiO_4 crystal well matched with JCPDS 79-1910 and 37-1485,

respectively. It means that $Zn_2SiO_4:Mn^{2+}$ phosphor shell successfully formed on SiO_2 powder surface through thermal diffusion and reaction between ZnO, MnO and SiO_2 powder as appear by SEM images in figure 30. Figure 32 shows XRD peaks of (101) plane of hexagonal SiO_2 crystal.

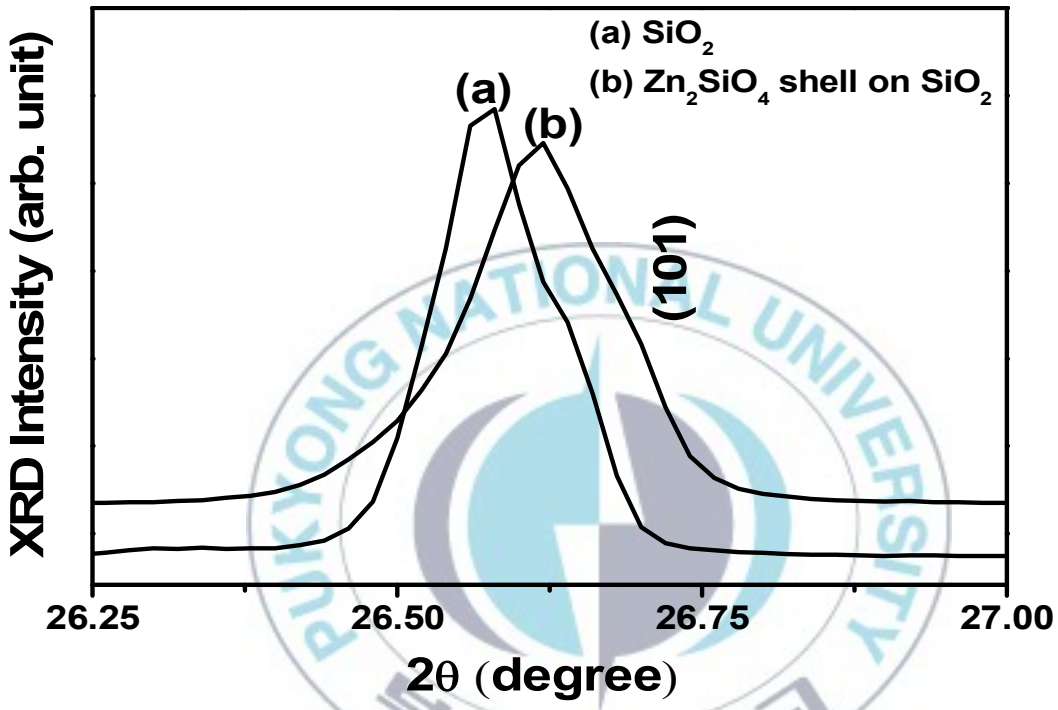

Figure 32. XRD peak of SiO_2-(101) crystal plane of (a) SiO_2 and (b) $Zn_2SiO_4:Mn^{2+}$ phosphor shell on SiO_2.

Peak position of SiO_2-(101) plane is shifted to large angle. It means lattice contraction of SiO_2 crystal. It can be explained that lattice space of ZnO ($d_{(002)}$ = 2.5938 Å) is smaller than that of

SiO_2 ($d_{(101)}$ = 3.3438 Å) therefore, lattice matching between ZnO and SiO_2 occur for formation of stable Zn_2SiO_4 crystal ($d_{(113)}$ = 2.8350 Å). Figure 33 shows XRD peak of (113) plane with increasing Mn^{2+} concentration in Zn_2SiO_4:Mn^{2+} crystal.

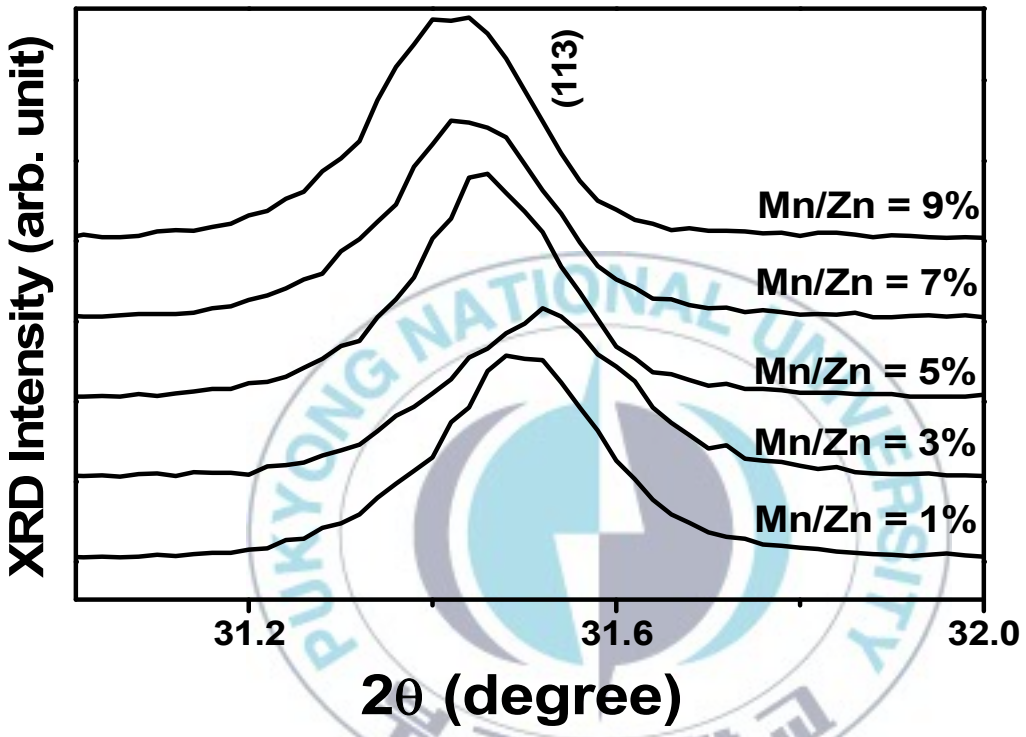

Figure 33. XRD peak of (113) crystal plane of Zn_2SiO_4:Mn^{2+} phosphor shell on SiO_2 as a function of Mn^{2+} concentration.

Peak position of (113) plane shift to low angle as increasing Mn^{2+} concentration. It is due to the lattice expansion caused by substitution of slightly large Mn^{2+} (0.80Å) ions in small Zn^{2+}

(0.74Å)site.

Figure 34 shows PL spectra of formed $Zn_2SiO_4:Mn^{2+}$ phosphor shell as function of Mn^{2+} concentration.

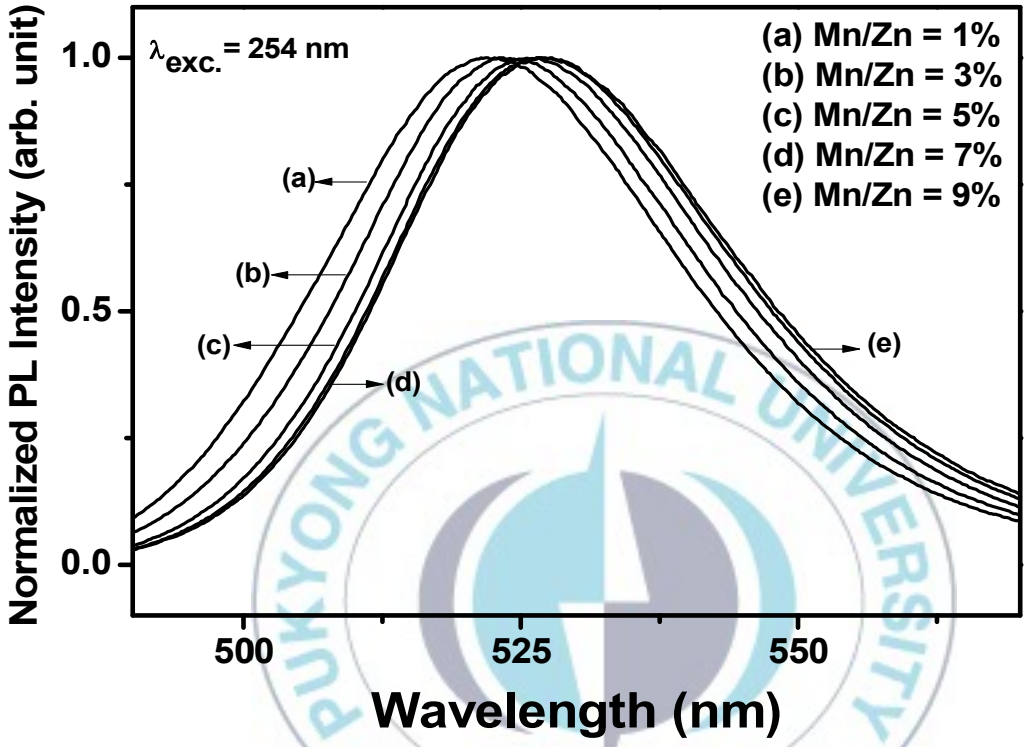

Figure 34. Normalized PL spectra of $Zn_2SiO_4:Mn^{2+}$ phosphor shell on SiO_2 as a function of Mn^{2+} concentration.

PL spectra show green emission due to atomic transition from $^4T_1$ to $^6A_1$ in d-orbital of Mn^{2+} ions. Emission peak position of $Zn_2SiO_4:Mn^{2+}$ phosphor shell shift from 521nm to 526 nm with increasing Mn^{2+} concentration in $Zn_2SiO_4:Mn^{2+}$. It can be explained

that crystal field strength increase with increasing Mn^{2+} concentration as appear ESR spectra of figure 35.

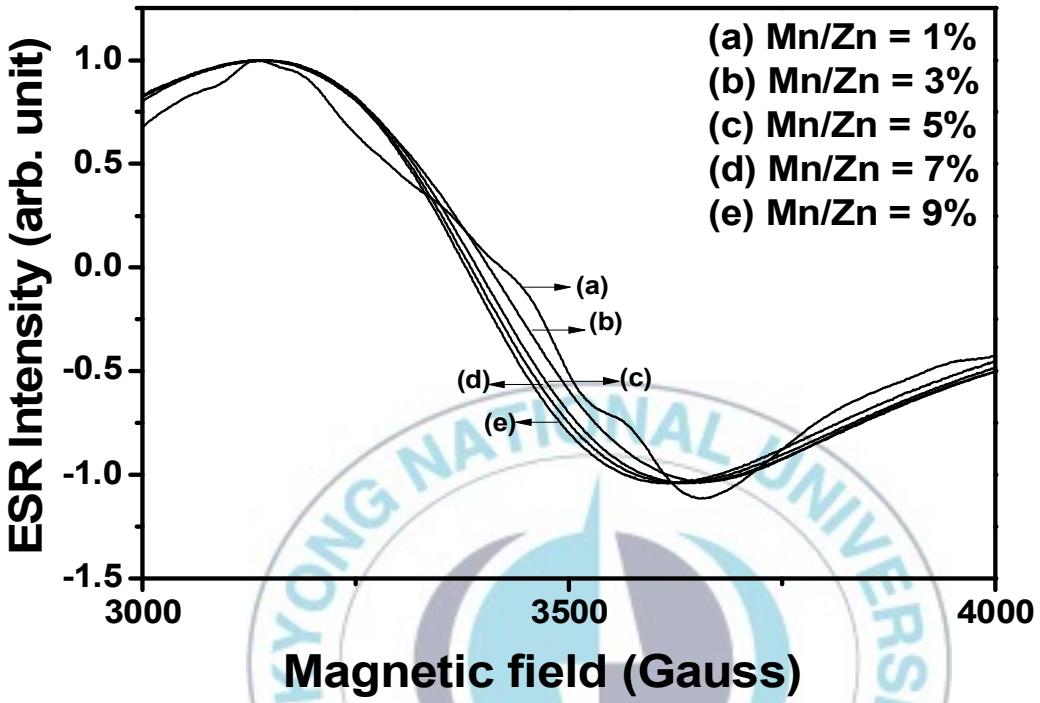

Figure 35. ESR spectra of $Zn_2SiO_4:Mn^{2+}$ phosphor shell on SiO_2 as a function of Mn^{2+} concentration.

From ESR spectra, g factor increase with increasing Mn^{2+} concentration shown in figure 36.

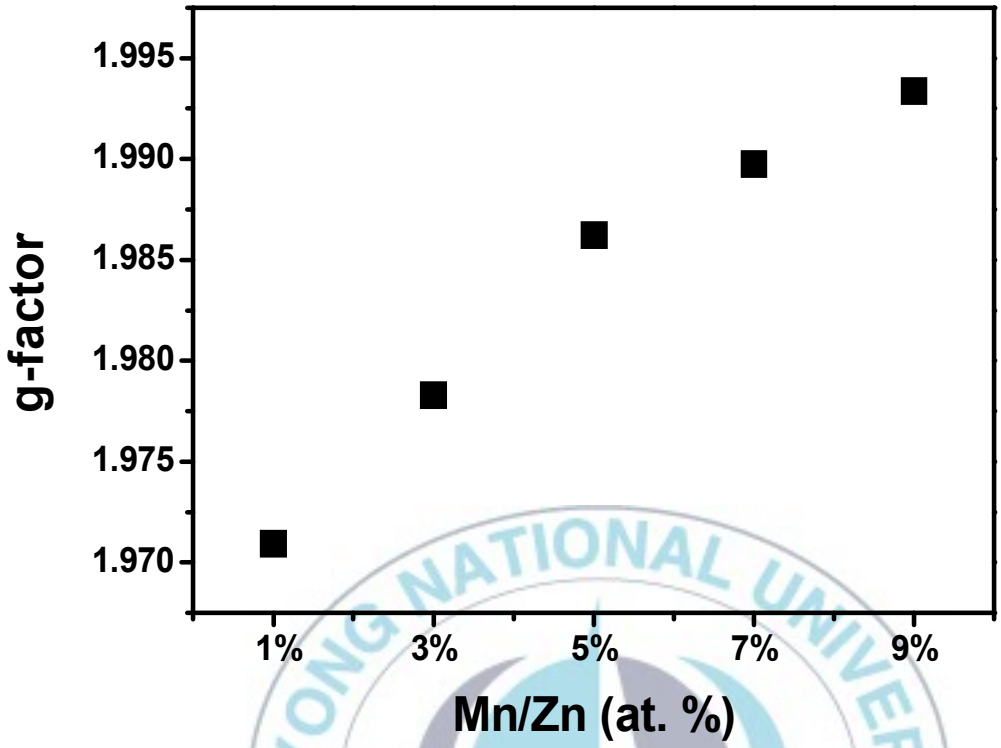

Figure 36. g factor of Zn_2SiO_4:Mn^{2+} phosphor shell on SiO_2 as a function of Mn^{2+} concentration.

Increasing g factor means increase of crystal field strength as following expression[58].

$$g = 2.0023 - \alpha^2 \frac{8\lambda_{(fr.Ion)}}{\Delta}$$

Where α^2 is the coefficient giving the mixing of orbitals $d_{x^2-y^2}$ and d_{z^2} of metal ion with the ligand, $\lambda_{(fr.Ion)}$ is the spin-orbit coupling constant for the free ion and Δ is crystal field.

Therefore red shift of PL with increasing Mn^{2+} ions concentration due to increase of crystal field according to the Tanabe-Sugano diagram[2].

Figure 37 shows decay curve of $Zn_2SiO_4:Mn^{2+}$ phosphor shell as function of Mn^{2+} concentration.

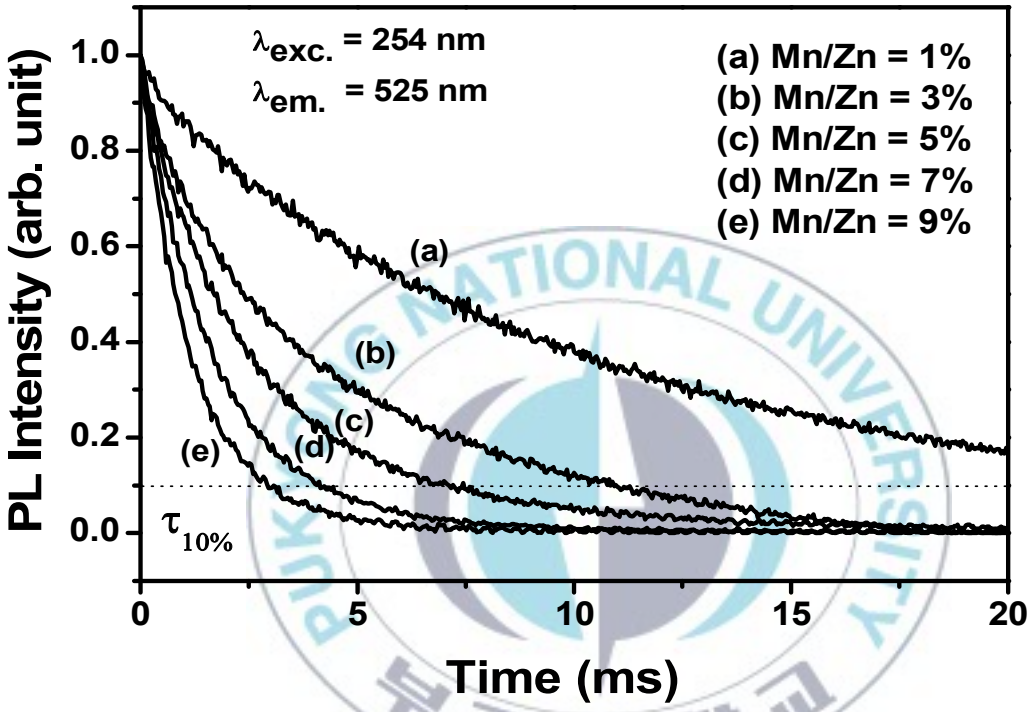

Figure 37. Decay curves of $Zn_2SiO_4:Mn^{2+}$ phosphor shell on SiO_2 as a function of Mn^{2+} concentration.

Decay time decreases from 20 ms to 2.8 ms with an increase in the Mn^{2+} concentration. This short decay time with increasing Mn^{2+} concentration have been explained that Mn-Mn exchange

interaction or Mn–Mn pairing[40,44]. Generally, decay time of $Zn_2SiO_4:Mn^{2+}$ phosphor shell is short compared to conventional powder phosphor reported by other researchers[44,56]. These behaviors can be explained by morphology of formed $Zn_2SiO_4:Mn^{2+}$ phosphor shell on SiO_2 powder. Dense and closely packed shape of $Zn_2SiO_4:Mn^{2+}$ phosphor shell in limited area can give stress to Mn^{2+} ions. This stress affects forbidden transition of Mn^{2+} ions in $Zn_2SiO_4:Mn^{2+}$ and give rise to short decay time due to relaxation of forbidden transition of Mn^{2+} ions.

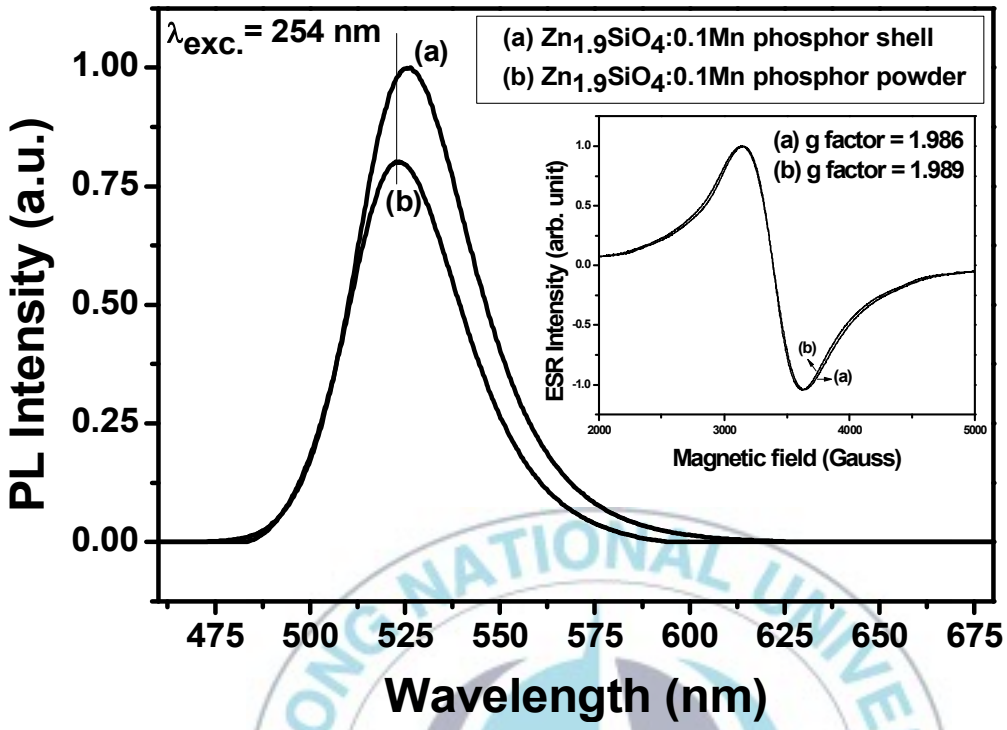

Figure 38. PL spectra of (a) $Zn_2SiO_4:Mn^{2+}$ phosphor shell on SiO_2 and (b) conventional synthesized $Zn_2SiO_4:Mn^{2+}$ phosphor powder at the same Mn^{2+} concentration (Mn/Zn = 5 %). The inset shows ESR spectra.

Figure 38 shows PL and ESR spectra of $Zn_2SiO_4:Mn^{2+}$ phosphor shell and conventional synthesized $Zn_2SiO_4:Mn^{2+}$ phosphor powder at same Mn^{2+} concentration. PL peak position of phosphor shell shift to red compared to phosphor powder. It means that crystal field strength of phosphor shell increase compared to phosphor powder according to the Tanabe-Sugano diagram.

However, g factor of phosphor shell lower than that of phosphor powder as seen in ESR spectra of figure 38. Thus red shift of phosphor shell can not be explained by crystal field. This behavior can be explained local stress of Mn^{2+} due to the lattice strain. Figure 39 show XRD patterns of Zn_2SiO_4:Mn^{2+} phosphor shell and Zn_2SiO_4:Mn^{2+} phosphor powder at same Mn^{2+} concentration. XRD peak position of phosphor shell shift to low angle compared to phosphor powder. It means that phosphor shell have expansion and distortion directed to (113) plane and give stress to localized Mn^{2+} ions. Figure 40 and 41 show decay curves and PLE spectra of Zn_2SiO_4:Mn^{2+} phosphor shell and Zn_2SiO_4:Mn^{2+} phosphor powder at same Mn^{2+} concentration. Decay time of phosphor shell (7.3 ms) is shorter than that of phosphor powder (12 ms). This behavior can be explained that phosphor shell have local stress and this stress affects transition of Mn^{2+} ions. PLE spectra show direct evidence of relaxation of Mn^{2+} transition in phosphor shell, which reveal that signals of forbidden transition in Mn^{2+} ions is significantly higher than that of phosphor powder.

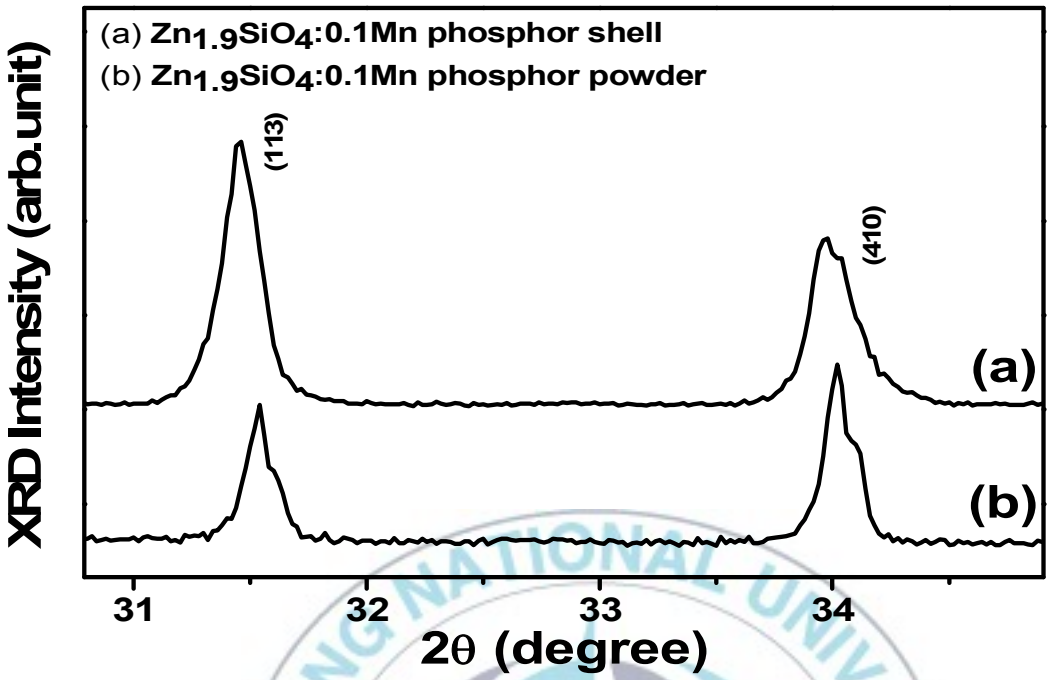

Figure 39. XRD patterns of (a) $Zn_2SiO_4:Mn^{2+}$ phosphor shell on SiO_2 and (b) conventional synthesized $Zn_2SiO_4:Mn^{2+}$ phosphor powder at the same Mn^{2+} concentration (Mn/Zn = 5 %).

Especially, the excitation intensity is shown in near UV region (350~375 nm) and blue region (420~470 nm), $Zn_2SiO_4:Mn^{2+}$ phosphor shell on SiO_2 powder can be applied to green component for white-LED using near UV and blue LED chip as well as display devices.

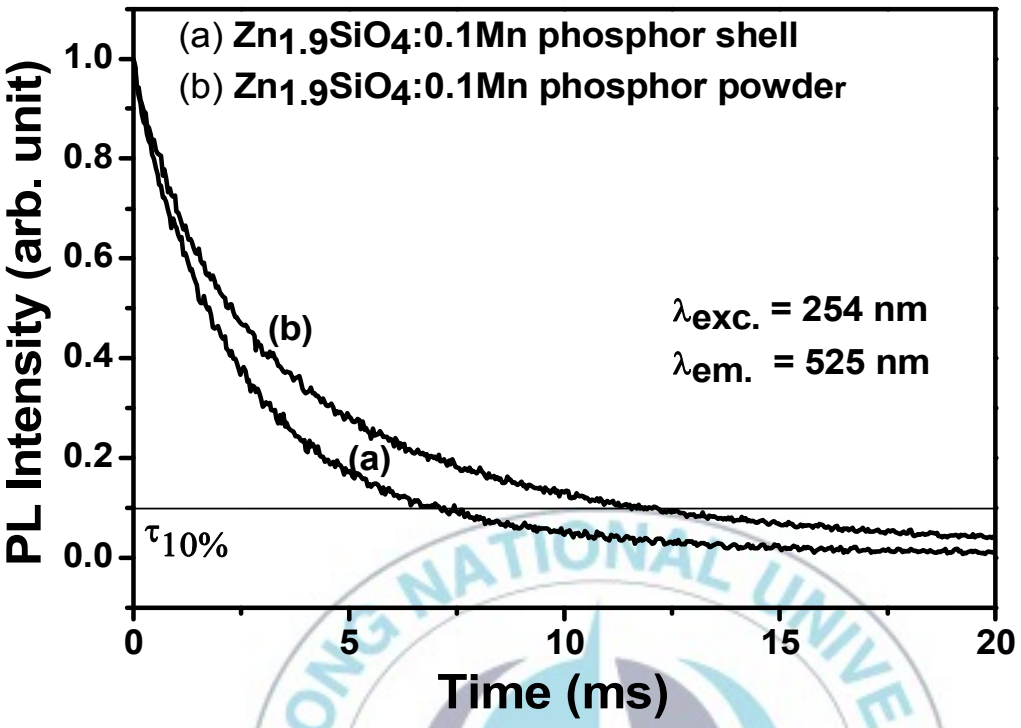

Figure 40. Decay curves of (a) $Zn_2SiO_4:Mn^{2+}$ phosphor shell on SiO_2 and (b) conventional synthesized $Zn_2SiO_4:Mn^{2+}$ phosphor powder at the same Mn^{2+} concentration (Mn/Zn = 5 %).

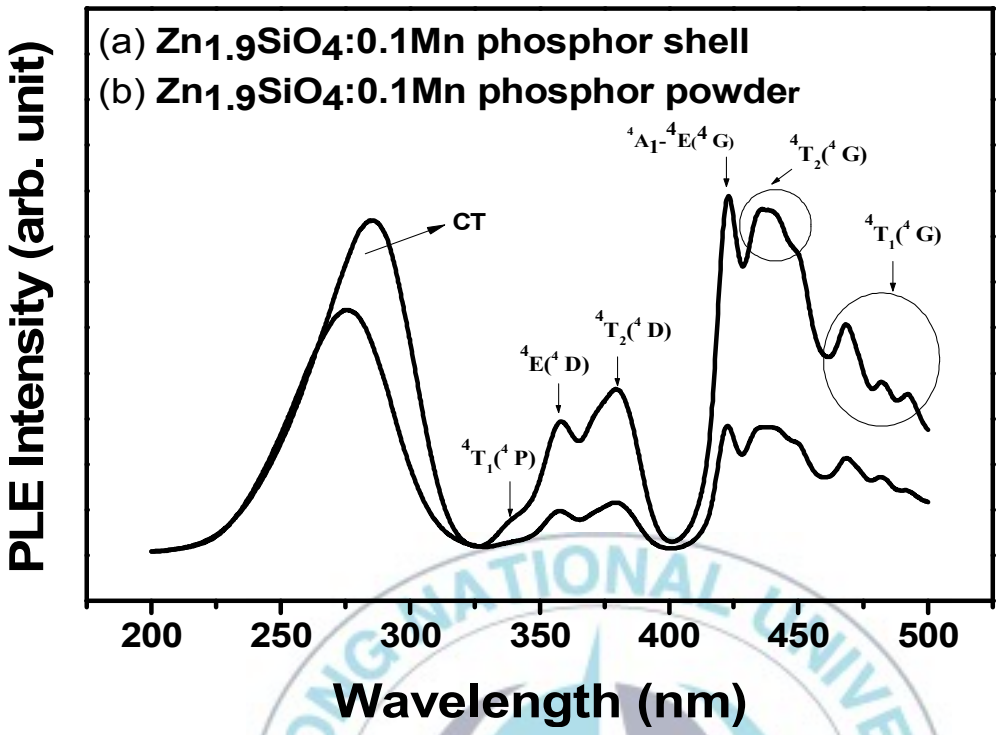

Figure 41. PLE spectra of (a) $Zn_2SiO_4:Mn^{2+}$ phosphor shell on SiO_2 and (b) conventional synthesized $Zn_2SiO_4:Mn^{2+}$ phosphor powder at the same Mn^{2+} concentration (Mn/Zn = 5 %).

5.3. $BaSi_2O_5:Eu^{2+}$ FILM PHOSPHOR

Figure 42 shows the formation procedure of $BaSi_2O_5:Eu^{2+}$ thin-film phosphor and scanning electron microscope (SEM) images of spin-coated $Ba_{1-x}Eu_xO$ thin-film and formed $BaSi_2O_5:Eu^{2+}$ thin-film phosphor on SiO_2 substrate after annealing.

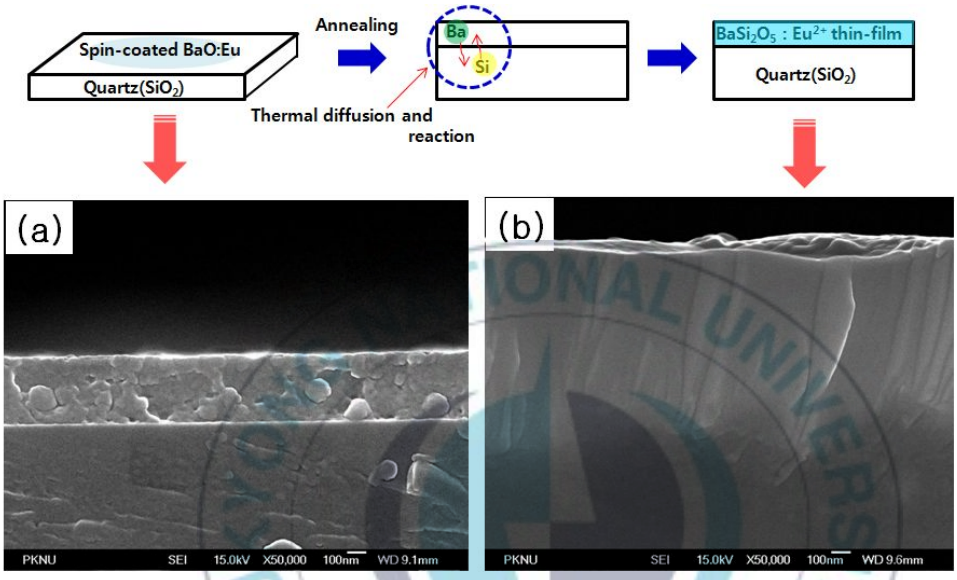

Figure 42. Schematic of formation procedure of $BaSi_2O_5:Eu^{2+}$ thin-film phosphor and cross-section SEM images of (a) as-grown (b) annealed film.

SEM images present that spin-coated $Ba_{1-x}Eu_xO$ thin-film has 300 nm thickness with rough shape and formed $BaSi_2O_5:Eu^{2+}$ thin-film phosphor has 800 nm thickness with smooth and densely packed shape. Also, interface of thin-film and substrate is not clear in formed $BaSi_2O_5:Eu^{2+}$ thin-film phosphor while that of spin-coated

$Ba_{1-x}Eu_xO$thin-film is clear. It is due to the diffusion reaction between thin-film and substrate at interface.

Figure 43 shows XRD patterns of $BaSi_2O_5:Eu^{2+}$ thin-film phosphor as a function of annealing temperature.

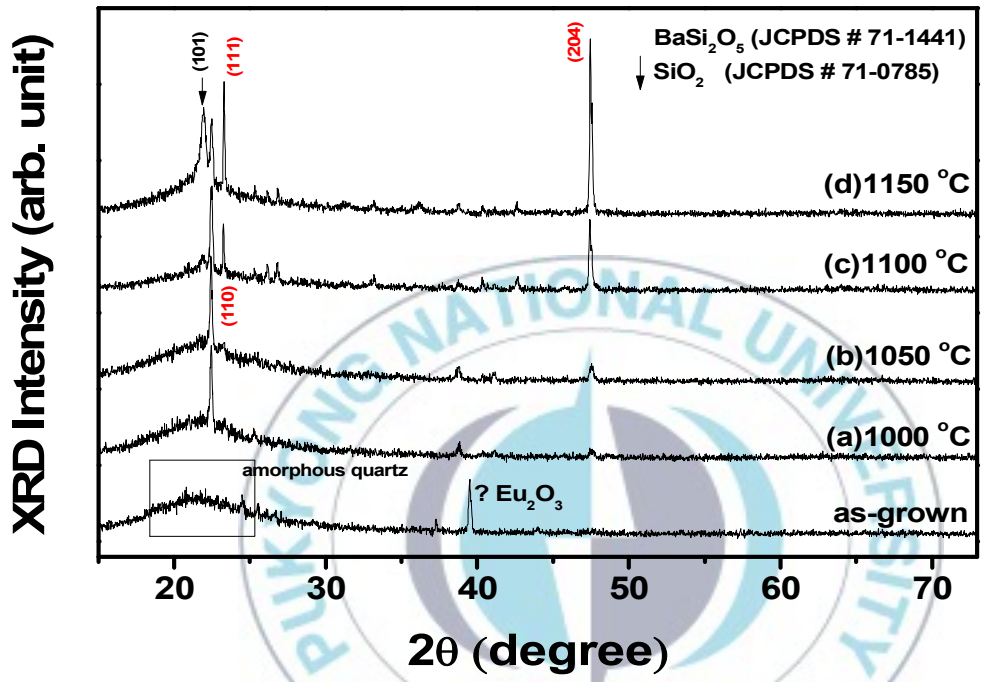

Figure 43. XRD patterns of $BaSi_2O_5:Eu^{2+}$ thin-film phosphor as a function of annealing temperature fixed annealing time (5 hr) and Eu^{2+} concentration (Eu/Ba = 11 %).

Abroad peak around $2\theta = 21^{\circ}$ which is from amorphous SiO_2 substrate. All annealed sample well matched with $BaSi_2O_5$ crystal (JCPDS file 71-1441) which means that between spin-coated

BaEuO thin-film and SiO_2 substrate successfully reacted during annealing and $BaSi_2O_5:Eu^{2+}$ thin-film formed on SiO_2 substrate as seen in SEM images of figure 42. And they have some preferred crystalline which is revealed (110), (111), (204) crystal plane. Increasing the annealing temperature peak intensity of (204) crystal plane is dominantly increased and reveal (111) crystal plane at 1100, 1150 °C annealed sample. Also, (101) peak related cristobalite phase appears at 1150 °C annealed sample. It is due to the transition from amorphous SiO_2 substrate to crystallized SiO_2 with increasing annealing temperature.

Figure 44 shows PL spectra of $BaSi_2O_5:Eu^{2+}$ thin-film phosphor excited by 365 nm UV-lamp as a function of annealing temperature. All sample broad-green emission peaking at 510 nm which is originated from the 5d-4f transition of Eu^{2+} ions due to the strong coupling of 5d electrons with the host lattice. With increasing annealing temperature, PL intensities are significantly increased and then maximized at 1100 °C. Enhancement of PL with increasing annealing temperature can be explained crystalline character. From XRD patterns of figure 43 peak intensity of (204) plane of $BaSi_2O_5:Eu^{2+}$ thin-film is significantly increased with increasing annealing temperature. It means that PL properties of $BaSi_2O_5:Eu^{2+}$ thin-film are deeply related (204) crystal plane. Up to

1050 °C, crystallization of (204) crystal plan is poor and begin to appear (204) crystal plane at 1100 and 1150 °C annealed sample as seen in XRD patterns of figure 43.

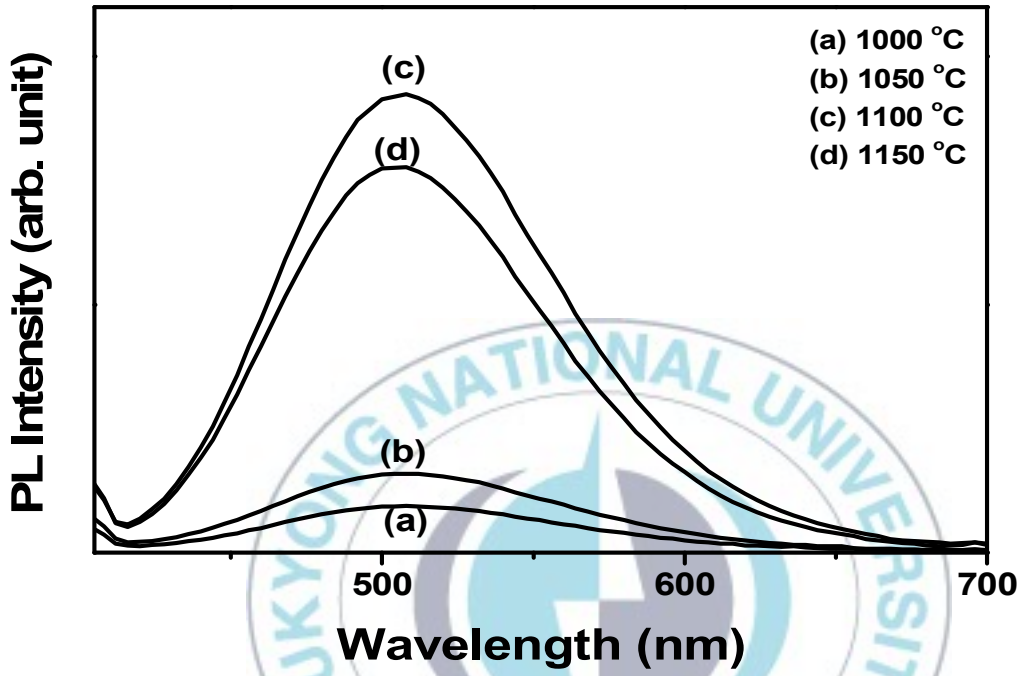

Figure 44. PL spectra of $BaSi_2O_5:Eu^{2+}$ thin-film phosphor as a function of annealing temperature fixed annealing time (5 hr) and Eu^{2+} concentration (Eu/Ba = 11 %).

PL properties Involving these crystalline character indicate that Eu^{2+} ions are selectively occupied and activated in (204) crystal plan of $BaSi_2O_5$ crystal. PL intensity of sample annealed at 1150 °C slightly decrease. It is due to the phase impurity (cristobalite) acting

luminescence killer.

Figure 45 shows XRD patterns of $BaSi_2O_5:Eu^{2+}$ thin-film as a function of annealing time fixed at annealing temperature of 1100 °C.

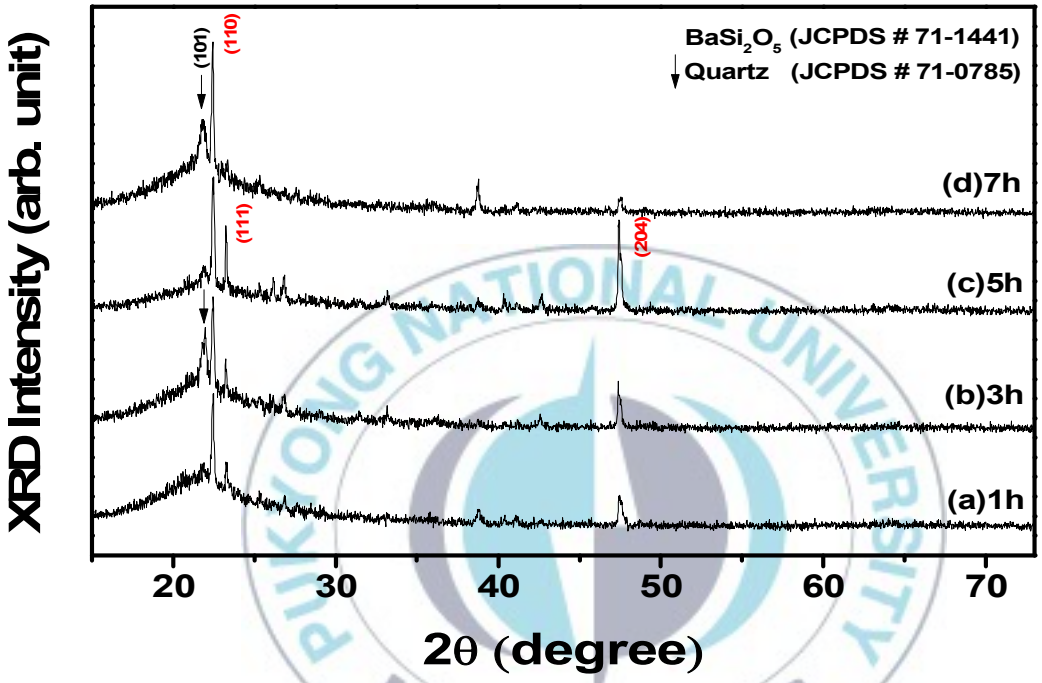

Figure 45. XRD patterns of $BaSi_2O_5:Eu^{2+}$ thin-film phosphor as a function of annealing time fixed annealing temperature (1100 ℃) and Eu^{2+} concentration (Eu/Ba = 11 %).

As increase of annealing time peak intensity of (204) crystal plane gradually increases and then significantly decreases in sample annealed for 7 hrs. In addition, XRD patterns revealed that (101)

crystal plane of cristobalite appear (3 hrs, 7 hrs annealed samples) and disappear (1 hr, 5 hrs annealed samples), it can be explained that cristobalite formed from amorphous SiO_2 react with $Ba_{1-x}Eu_xO$ thin-film during the annealing. These two components, i.e. $Ba_{1-x}Eu_xO$ and SiO_2 are competitively consumed. In other words, sample annealed for 1 hr has complete reaction between $Ba_{1-x}Eu_xO$ and crystallized SiO_2 (cristobalite) and sample annealed for 3hrs remain extra cristobalite after reaction between $Ba_{1-x}Eu_xO$ and crystallized SiO_2 (cristobalite). Also, samples annealed for 5, 7 hrs can be explained by these procedures.

Figure 46 shows PL spectra of $BaSi_2O_5:Eu^{2+}$ thin-film phosphors excited by 365 nm UV-lamp as a function of annealing time fixed at annealing temperature of 1100 ^oC. PL intensity of $BaSi_2O_5:Eu^{2+}$ thin-film phosphors gradually increase with increasing annealing time and then decrease in 7 hrs annealed sample. It can be explained that crystallinity of (204) crystal plane of $BaSi_2O_5$ crystal is enhanced with increasing the annealing time. Crystallinity of (204) crystal plane of sample annealed for 7 hrs abruptly decrease as seen in XRD patterns of figure 45. As seen in figure 46, PL intensity of sample annealed for 7 hrs significantly decrease caused by poor crystallinity of Eu^{2+} activated (204)-crystal plane.

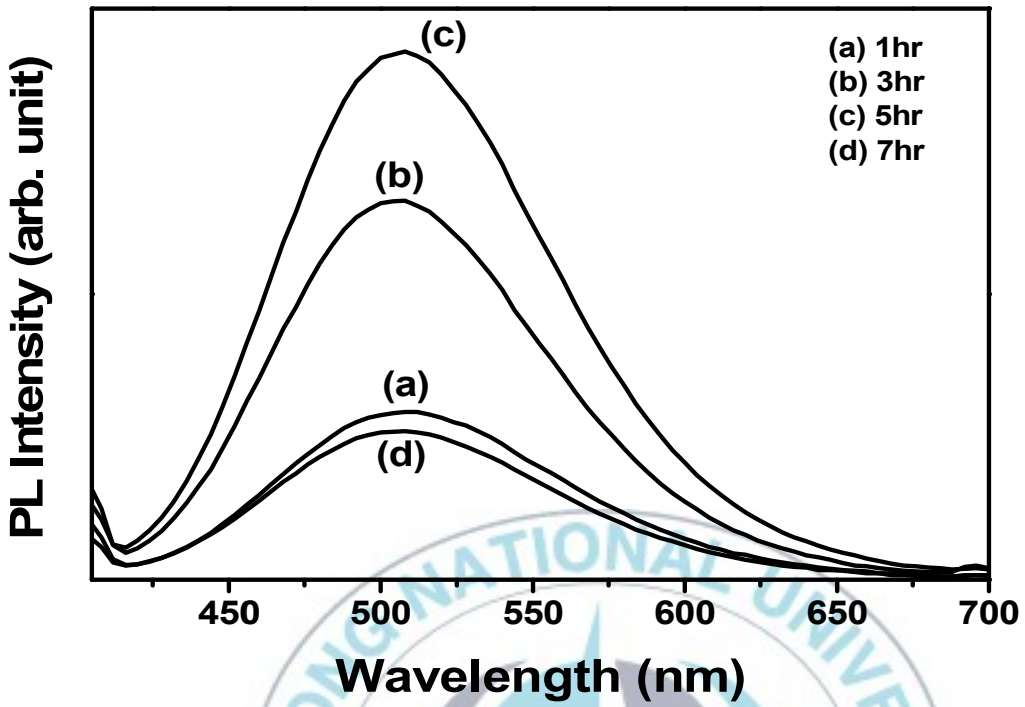

Figure 46. PL spectra of $BaSi_2O_5:Eu^{2+}$ thin-film phosphor as a function of annealing time fixed annealing temperature (1100 ℃) and Eu^{2+} concentration (Eu/Ba = 11 %).

Figure 47 and figure 48 show XRD patterns and PL spectra of $BaSi_2O_5:Eu^{2+}$ thin-film phosphors as a function of Eu^{2+} concentration fixed at annealing condition. XRD patterns reveal that Eu^{2+} ions affect growing $BaSi_2O_5$ crystal. As increase of Eu^{2+} concentration peak intensity of (204) crystal plane inreases and then decreases at Eu^{2+} concentration of 15 mol %. Also, PL intensity increases with increasing the Eu^{2+} concentration and then

decreases at Eu^{2+} concentration of 15 mol %. This PL properties agree well with crystallinity of (204) crystal plane as seen in XRD patterns of figure 48.

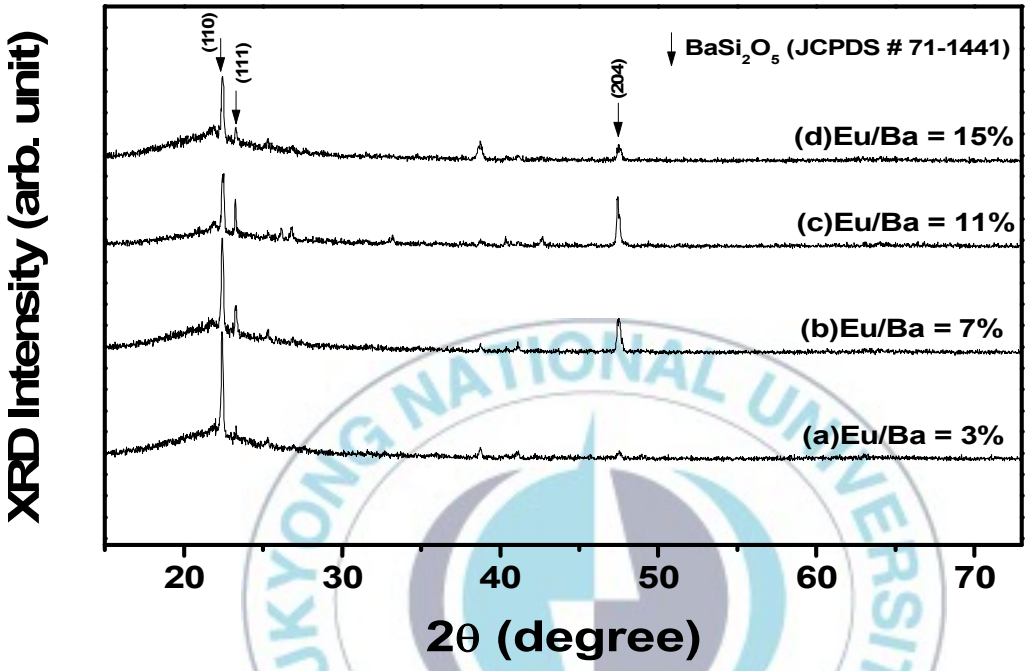

Figure 47. XRD patterns of $BaSi_2O_5:Eu^{2+}$ thin-film phosphor as a function of Eu^{2+} concentration fixed annealing temperature (1100 ℃) and time (5 hr).

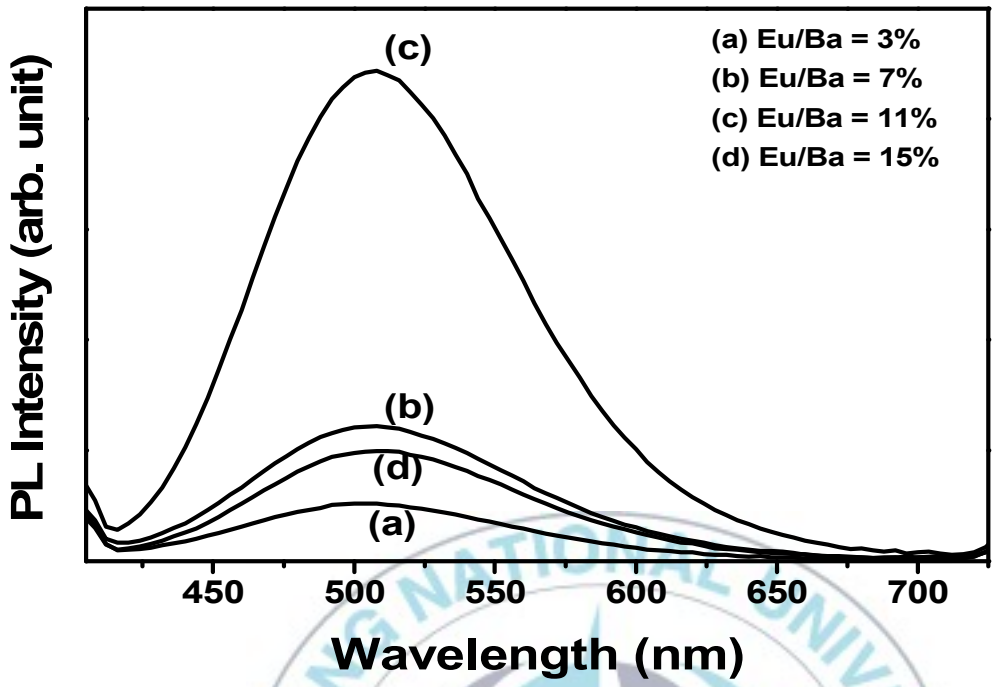

Figure 48. PL spectra of $BaSi_2O_5:Eu^{2+}$ thin-film phosphor as a function of Eu^{2+} concentration fixed annealing temperature (1100 ℃) and time (5 hrs).

PLE spectrum of $BaSi_2O_5:Eu^{2+}$ thin-film phosphor shows reasonable excitation in near UV region as seen in figure 49. Thus $BaSi_2O_5:Eu^{2+}$thin-film phosphor has applicability of green component for white LED using near UV.

Figure 50 shows photograph of our bright-transparence $BaSi_2O_5:Eu^{2+}$ thin-film phosphor on quartz substrate excited by 365 nm UV lamp under day light lamp. These excellent luminance properties can be explained by morphology and unique crystalline

of $BaSi_2O_5:Eu^{2+}$ thin-film phosphor. Dense and closely packed shape of film reduce luminescence killer such as pores, grain boundaries and effectively absorb excitation wavelength.

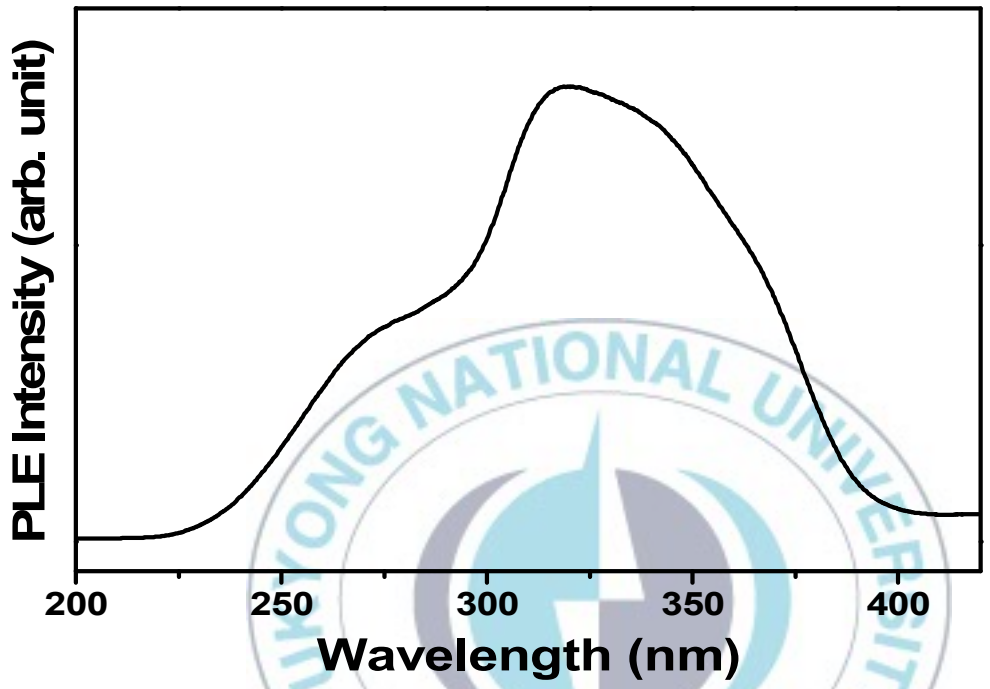

Figure 49. PLE spectra of $BaSi_2O_5:Eu^{2+}$ thin-film phosphor annealed at 1100 ℃ for 5 hrs.

In addition, directed crystalline reduce boundaries between grains. These factors affect optical properties of thin-film phosphor. Generally, the transparency of a ceramics is limited by light scattering from grain boundaries or pores[52].

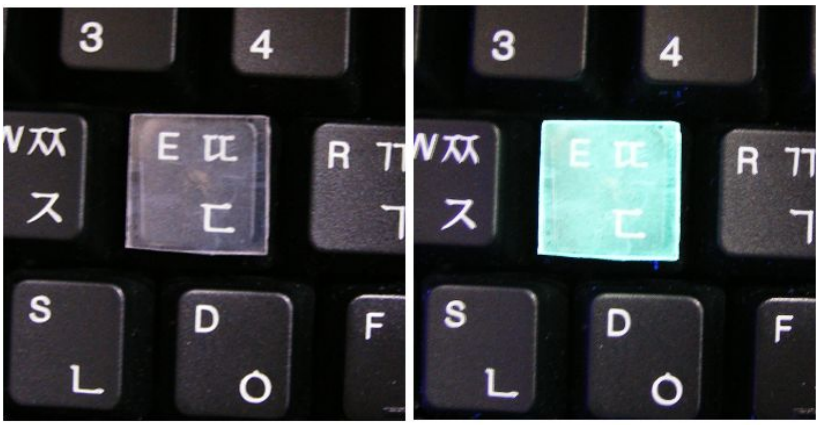

Figure 50. Photograph of $BaSi_2O_5:Eu^{2+}$ thin-film phosphor under day light lamp.

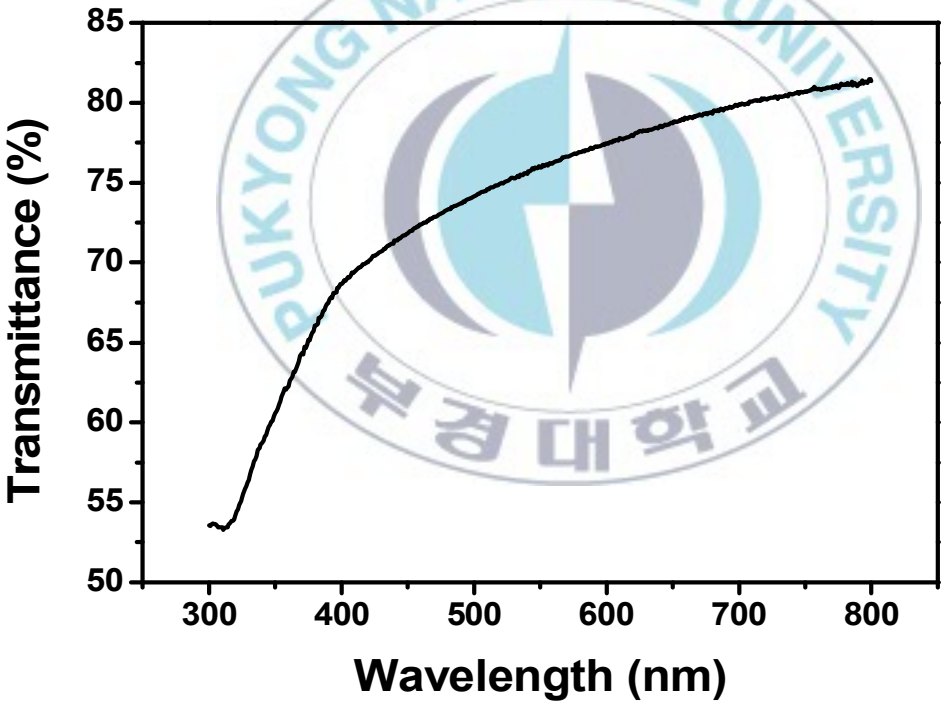

Figure 51. Transmittance spectrum of $BaSi_2O_5:Eu^{2+}$ thin-film phosphor.

Transmittances of $BaSi_2O_5:Eu^{2+}$ thin-film phosphor revealed 75 % at visible wave length range as seen in figure 51. It is due to reduction of scattering by reducing grain boundaries and pores.

6. CONCLUSIONS

Our studies on super bright-transparent film phosphors can be summarized as followings.

(1) $Zn_2SiO_4:Mn^{2+}$ phosphor films on quartz glass substrates were fabricated by the thermal diffusion of 800-nm-thick ZnO:Mn films, spreading out to a depth of about 1000 nm at 1100 °C. The inverse of decay time from Mn^{2+} showed the same increasing trend as the degree of texture as a function of annealing temperature. The brightest $Zn_2SiO_4:Mn^{2+}$ film (Mn/Zn = 5 at.%) resulted from annealing at 1100 °C and exhibited a PL brightness of 65% and 40 % excited by 254 nm and 147 nm compared with a commercially available $Zn_2SiO_4:Mn^{2+}$ phosphor powder, respectively. A maximum transparency of 70%, and a very short decay time of $\tau_{10\%}$ = 4.4 ms. These excellent properties can be attributed to the unique textured structure and continuous grading of the interface chemical composition. Although the sample annealed at 1200 °C showed the best properties in terms of texture degree and inverse decay time, its PL intensity is much too low for practical use owing to the pronounced sublimation of ZnO:Mn at the surface. If this vaporization can be prevented using an appropriate high-pressure ambient gas, it is considered that a higher PL intensity can be

achieved for the sample annealed at 1200 °C than for the brightest sample annealed at 1100 °C.

(2) $Zn_2SiO_4:Mn^{2+}$ phosphor layer successfully formed on surface of SiO_2 powder through thermal-diffusion reaction between SiO_2 powder and $Zn_{1-x}Mn_xO$ powder. Formed $Zn_2SiO_4:Mn^{2+}$ phosphor layer showed short decay time ($\tau_{10\%}$ = 7.3 ms) compared to that of phosphor powder ($\tau_{10\%}$ = 12 ms) at same Mn^{2+} concentration (Mn/Zn = 5 %). From excitation spectrum, we confirmed that forbidden transition of Mn^{2+} ions was relaxed. It is can be explained local stress of Mn^{2+} ions due to the lattice strain and distortion.

(3) $BaSi_2O_5:Eu^{2+}$ thin-film phosphors were grown on quartz substrate using simple method through thermal-diffusion reaction between quartz substrate and spin-coated BaO:Eu thin-film (300 nm) on quartz substrate. $BaSi_2O_5:Eu^{2+}$ thin-film (800 nm) phosphors formed on quartz revealed preferred crystalline [(110), (111), (204)-crystal plane] as well as dense and closely packed shape. These unique structure and morphology profoundly linked to luminescent and optical properties. Transmittances of $BaSi_2O_5:Eu^{2+}$ thin-film phosphor revealed 75 % at visible wave length range. In addition, Eu^{2+} ions affect growing the $BaSi_2O_5$ crystal and have activated preferred crystal plane [(204)-crystal plane] in $BaSi_2O_5$

crystal.

REFERENCES

[1] W.M.Yen, S.Shionoya, H.Yamamoto, Phosphor Handbook, 2nd ed., CRC Press, Boca Raton, (2007).

[2] G.Blasse, B.C.Grabmaier, Luminescent Materials, Springer-Verlag, Berlin, (1994).

[3] T.Hase, T.Kano, E.Nakazawa, H.Yamamoto, Advanced in Electronics and Electron Physics, 79, 271 (1990).

[4] M.R.Royce, U.S. Pat., 3, 418, 246 (1968).

[5] S. Woodcock and J.D.Leyland, Displays, 69 (1979).

[6] S. L. Jones, D. Kumar, K. G. Cho, R. Singh, and P. H. Holloway, Displays, 19, 151 (1999).

[7] Y. R. Do, Y. C. Kim, S. H. Cho, J. H. Ahn, and J. G. Lee, Appl. Phys. Lett., 82, 4172 (2003).

[8] K. G. Cho, D. Kumar, D. G. Lee, S. L. Jones, P. H. Holloway, and R. K. Singh, Appl. Phys. Lett., 71, 3335 (1997).

[9] Philip D. Rack and Paul H. Holloway, Materials Science and Engineering, R21, 171 (1998).

[10] J. A. Duffy, Bonding, Energy levels and Bands in Inorganic Solids, Wiley, NY, 1990.

[11] S. S. Zumdahl, Chemistry Second Edition, DC Health and Company, Lexington, 1989.

[12] Gerloch, R. C. Slade, Ligand-Field Parameters, Cambridge

University Press, London, 1973.

[13] D. R. Askeland, The Science and Engineering of Materials, PWS Publishing, Boston, MA, 1994.

[14] R.C. Ropp, Luminescence and the solid state, Elsevier, NY, 1991.

[15] Y.R.Do, Y.C.Kim, D.H.Park, and Y.D.Huh, J. Electrochem. Soc., 152 (4), H48-H52 (2005).

[16] K.G.Cho, D.Kumar, S.L.Jones, D.G.Lee, P.H.Holloway, and R.K.Singh, J. Electrochem. Soc. 145, 3456 (1998).

[17] Jurgen R.Meyer-Arendt, Introduction to classical and modern optics, Prentice-Hall, Inc., New Jersey, 1995.

[18] J. D. Joannopoulos, P. R. Villeneuve, and S. Fan, *Nature (London)*, 386, 143 (1997).

[19] M. Boroditsky, T. F. Krauss, R. Coccioli, R. Vrijen, R. Bhat, and E. Yablonovitch, *Appl. Phys. Lett.*, 75, 1036 (1999).

[20] H.-Y. Ryu, J.-K. Hwang, Y.-J. Lee, and Y.-H. Lee, *IEEE J. Sel. Top. Quantum Electron.*, 8, 238 (2002).

[21] B. J. Matterson, J. M. Lupton, A. F. Safonov, M. G. Salt, W. L. Barnes, and I. D. W. Samuel, *Adv. Mater. (Weinheim, Ger.)*, 13, 123 (2001).

[22] T. Maple and R. Buchanan, *J. Vac. Sci. Technol.*, 10, 616 (1973).

[23] C. Sella, J. Martin, and Y. Charreire, *Thin Solid Films*, 90,

181 (1982).

[24] S. Y. Seo, S. Lee, H. D. Park, N. Shin, and K.-S. Sohn, *J. Appl. Phys.*, 92, 5248 (2002).

[25] J. S. Bae, J. H. Jeong, S.-S. Yi, and J.-C. Park, *Appl. Phys. Lett.*, 82, 3629 (2003).

[26] K.S.Shon, N.S.Shin, Y.C.Kim, Y.R.Do, Appl. Phyys. Lett., 85, 55 (2004).

[27] Y.K.Lee, J.Y.Cho, C.R.Park, Y.D.Huh, Y.C.Kim, and Y.R.Do, Electrochem. Solid-State Lett., 10 (3), H82-H84 (2007).

[28] K.N.Lee, J.H.Moon, J.H.Oh, and Y.R.Do, J. Electrochem. Soc., 156 (9) J283-J287 (2009).

[29] W.H.Chao, R.J.Wu, C.S.Tsai, and T.B.Wu, J. Electrochem. Soc., 156 (12), J370-J374 (2009).

[30] W.H.Chao, R.j.Wu, C.S.Tsai, and T.B.Wu, J. Appl. Phys.,107, 0131101 (2010).

[31] K. C. Misbra, J. K. Berkowitz, K. H. Johnson, and P. C. Schmidt, *Phys. Rev. B*, 45, 10902 (1992).

[32] S.-S. Yi, J. S. Bae, B. K. Moon, J. H. Jeong, J.-C. Park, and I. W. Kim, *Appl. Phys. Lett.*, 81, 3344 (2002).

[33] S.-S. Yi, J. S. Bae, K. S. Shin, J. H. Jeong, J.-C. Park, and P. H. Holloway, *Appl. Phys. Lett.*, 84, 353 (2004).

[34] D. S. Zhang, K. Y. Ko, H. K. Park, D. H. Yoon, and Y. R.

Do, J. Electrochem. Soc., 155 (5), J111 (2008).

[35] K. I. Seo, J. H. Park, J. S. Kim, Y. H. Na, J. C. Choi, and J. S. Bae, Solid State Commun., 149, 1578 (2009).

[36] M. Marinsek, K. Zupan, and J. Maeek, J. Power Sources., 106, 178 (2002).

[37] T. Minami, Y. Kuroi, and S. Takata, J. Vac. Sci. Technol. A, 14, 1736 (1996).

[38] F. Marumo, Y. Syono, Acta Crystallographica B 27, 1868 (1971).

[39] N.Yocom, R.S.Meltzer, K.W.Jang, M.G.Rim, J.Soc. Inform. Display., 4, 169 (1996).

[40] C.R.Ronda, T. Amrein, J. Lumin., 69, 245 (1996).

[41] H. Chang, H.D.Park, K.S.Sohn, J.D.Lee, J. Kor. Phys. Soc., 34, 545 (1999).

[42] A. H. Kitai: Thin Solid Films 445, 367 (2003).

[43] T. Minami, T. Miyata, S. Takata, and I. Fukuda: Jpn. J. Appl. Phys. 30, L117 (1991).

[44] C. Barthou, J. Benoit, P. Benalloul, and A. Morell, J. Electrochem. Soc., 141,524 (1994).

[45] R.M.Douglass, American Mineralogist 43, 517 (1958).

[46] W.M.Yen, M.J.Weber, Inorganic phosphors, CRC press 2004.

[47] S.H.M.Poort, A.Meeyerink, G.Blasse, J. Phys. Chem. Solids

58, 1451 (1997).

[48] S.H.M.Poort, G.Blasse, J. Lumin., 72, 247 (1997).

[49] C. S. Fuller and F. J. Morin, Phys. Rev., 105, 379 (1957).

[50] I.M.Svishchev, P.G.Kusalik, and V.V.Murashov, Phys. Rev. B 55, 721 (1997).

[51] D. Griinebaum, Th. Czekalla,, N. A. Stolwijk, H. Mehrer, I. Yonenaga, and K. Sumino, Appl. Phys. A 53, 65 (1991).

[52] R. Apetz and M. P. B. Bruggen, J. Am. Ceram. Soc., 86, 480 (2003).

[53] K. I. Seo, J. H. Park, J. S. Kim, G.C.Kim, and J.H.Yoo, J. Lumin., 128, 715 (2009).

[54] Z. Ji, L. Kun, S. Yongliang, and Y. Zhizhen, J. Cryst. Growth, 255, 353 (2003).

[55] J. Yan, Z. Ji, J. Xi, C. Wang, J. Du, and S. Zhao, Thin Solid Films 515, 1877 (2006).

[56] K. S. Sohn, B. H. Cho, and H. D. Park, J. Am. Ceram. Soc., 82, 2779 (1999).

[57] Y. Hao, Y. Wang, J. Lumin., 122-123, 1006 (2007).

[58] K. W. H. Stevens, Proc. R. Soc., A219, 542 (1953).

국문요약

On Super-Bright Transparent Film Phosphors
(고휘도 투명 필름형광체 연구)

본 연구에서는 석영기판(SiO_2)과 석영기판위에 스핀코팅법으로 형성된 필름(ZnO:Mn, BaO:Eu) 사이의 열확산 반응을 통해 필름형광체 ($Zn_2SiO_4:Mn^{2+}$, $BaSi_2O_5:Eu^{2+}$)를 합성하였다. X-선 회절패턴 분석 및 전자현미경 관찰을 통해 석영기판위에 필름형광체가 성공적으로 형성되었음을 확인하였고, 열처리 조건 및 활성제 농도에 따른 필름형광체의 발광 특성 및 광학적 특성을 조사하였다.

$Zn_2SiO_4:Mn^{2+}$ 필름형광체(두께 1 μm)는 (113), (223), (333) 결정면으로의 특정한 결정방향성을 가지며, 상용의 $Zn_2SiO_4:Mn^{2+}$ 분말형광체대비 65 %의 휘도를 나타내었다. 또한, 짧은 잔광시간 (4.4 ms)과 가시광 영역에서 70 %의 투명도를 나타내었다. SiO_2 분말위에 형성된 $Zn_2SiO_4:Mn^{2+}$ 형광체 막 (두께 5 μm)은 일반적인 $Zn_2SiO_4:Mn^{2+}$ 분말형광체와 비교했을 때 짧은 잔광시간을 나타내었다. $BaSi_2O_5:Eu^{2+}$ 필름형광체 (두께 800 nm)는 (110), (111), (204) 결정면으로의 결정성을

가지며, 가시광 영역에서 75 % 의 투명도를 나타내었다.

핵심되는 말 : 필름형광체, 투명도